



Experiments and modeling of iron-particle-filled magnetorheological elastomers

K. Danas^{a,*}, S.V. Kankanala^{b,1}, N. Triantafyllidis^{a,c,d}

^a Laboratoire de Mécanique des Solides, C.N.R.S. UMR7649 & Département de Mécanique, École Polytechnique, ParisTech, 91128 Palaiseau Cedex, France

^b BD Technologies, 21 Davis Drive, Research Triangle Park, NC 27709, USA

^c Aerospace Engineering Department, The University of Michigan, Ann Arbor, MI 48109-2140, USA

^d Mechanical Engineering Department, The University of Michigan, Ann Arbor, MI 48109-2140, USA

ARTICLE INFO

Article history:

Received 3 March 2011

Received in revised form

6 September 2011

Accepted 18 September 2011

Available online 22 September 2011

Keywords:

Magnetorheological elastomers

Magnetomechanical processes

Finite strain

Energy methods

Nonlinear elasticity

ABSTRACT

Magnetorheological elastomers (MREs) are ferromagnetic particle impregnated rubbers whose mechanical properties are altered by the application of external magnetic fields. Due to their coupled magnetoelastic response, MREs are finding an increasing number of engineering applications. In this work, we present a combined experimental and theoretical study of the macroscopic response of a particular MRE consisting of a rubber matrix phase with spherical carbonyl iron particles. The MRE specimens used in this work are cured in the presence of strong magnetic fields leading to the formation of particle chain structures and thus to an overall transversely isotropic composite. The MRE samples are tested experimentally under uniaxial stresses as well as under simple shear in the absence or in the presence of magnetic fields and for different initial orientations of their particle chains with respect to the mechanical and magnetic loading direction.

Using the theoretical framework for finitely strained MREs introduced by Kankanala and Triantafyllidis (2004), we propose a transversely isotropic energy density function that is able to reproduce the experimentally measured magnetization, magnetostriction and simple shear curves under different prestresses, initial particle chain orientations and magnetic fields. Microscopic mechanisms are also proposed to explain (i) the counterintuitive effect of dilation under zero or compressive applied mechanical loads for the magnetostriction experiments and (ii) the importance of a finite strain constitutive formulation even at small magnetostrictive strains. The model gives an excellent agreement with experiments for relatively moderate magnetic fields but has also been satisfactorily extended to include magnetic fields near saturation.

© 2011 Elsevier Ltd. All rights reserved.

1. Introduction

Magnetorheological elastomers (MREs) are solids consisting of a rubber matrix filled with magnetizable particles, typically sub-micron sized iron particles (see Rigbi and Jilkén, 1983; Ginder et al., 1999). These composites are members of a wide class of materials, termed “*active materials*”, in virtue of their strong magnetoelastic coupling properties. More specifically, the application of an external magnetic field changes their mechanical properties, due to changes induced in

* Corresponding author.

E-mail addresses: kdanas@lms.polytechnique.fr, kosdanas@gmail.com (K. Danas), sundeep_kankanala@bd.com (S.V. Kankanala),

nick@lms.polytechnique.fr (N. Triantafyllidis).

¹ Former address: Research and Innovation Center, Ford Motor Company, Dearborn, MI 48109, USA.

their microstructure. An example is shown in Fig. 1, where the presence of a nondimensional magnetic field $h/\rho_0 M_s = 1$ (with ρ_0 and M_s denoting the initial density and saturation magnetization of the MRE, respectively) leads to an increase – compared to the absence of a magnetic field – in the stiffness of an MRE sample subjected to pure shear.

Since the mechanical properties of MREs can be altered rapidly and reversibly when subjected to external magnetic fields, these materials have been proposed and tested for a variety of applications in which it is desirable to continuously and controllably vary the effective stiffness of a device under different operating conditions. More specifically, MREs have been manufactured and studied as adaptive engine mounts and tunable shock absorbers (e.g., Ginder et al., 1999). In dealing with these materials, it has been observed that microstructure plays an important role in their macroscopic behavior. Motivated by the desire to enhance the magnetomechanical coupling of the resulting MRE composites, different microstructures have been created by the application of magnetic fields at curing. As one can see in Fig. 1, the particles in the MRE solid are arranged in a roughly column-like structure, with their orientation given by the vector \mathbf{N} , which coincides with the direction of the magnetic curing field. However, and in spite of several continuum as well as micromechanically based studies for MRE's, no combined experimental/theoretical study exists – to the best of the authors' knowledge – where an appropriate continuum framework for finite strain magnetoelasticity has been used to construct and validate an energy density for such solids, thus explaining the purpose of the present work.

Although a literature review of continuum as well as micromechanically based magnetoelasticity is beyond the scope of the present work, a few comments are helpful to put the present work in perspective and motivate the particular continuum model used here. While the majority of motivating experiments in MREs are relatively recent (see Jolly et al., 1996; Ginder et al., 1999, 2002; Bellan and Bossis, 2002; Gong et al., 2005; Coquelle et al., 2006), the continuum descriptions for the magnetoelastic response of solids go back to the 1950s and 1960s. The modeling approaches adopted can be broadly classified into two categories: (i) based on the “direct” method which uses conservation laws of continuum mechanics, e.g., Truesdell and Toupin (1960), Tiersten (1964), Maugin and Eringen (1972a,b), Pao and Yeh (1973), Pao (1978) and (ii) based on the “energy” method which uses the calculus of variations to extremize an appropriate potential energy, e.g., Tiersten (1965), Brown (1966), Maugin and Eringen (1972a,b). These approaches were developed independently of each other and, as expected, give different results for the Maxwell stresses, interface tractions and body forces according to the assumptions adopted in each case.

Recently, based on the work of Brown (1966), Kankanala and Triantafyllidis (2004) proposed a new coupled variational formulation for finite strain magnetoelasticity. By minimizing the model's generalized potential energy with respect to its independent variables, one obtains all the appropriate (mechanical as well as magnetic) governing equations and boundary/interface conditions. Moreover, it is shown by Kankanala and Triantafyllidis (2004) that the direct and

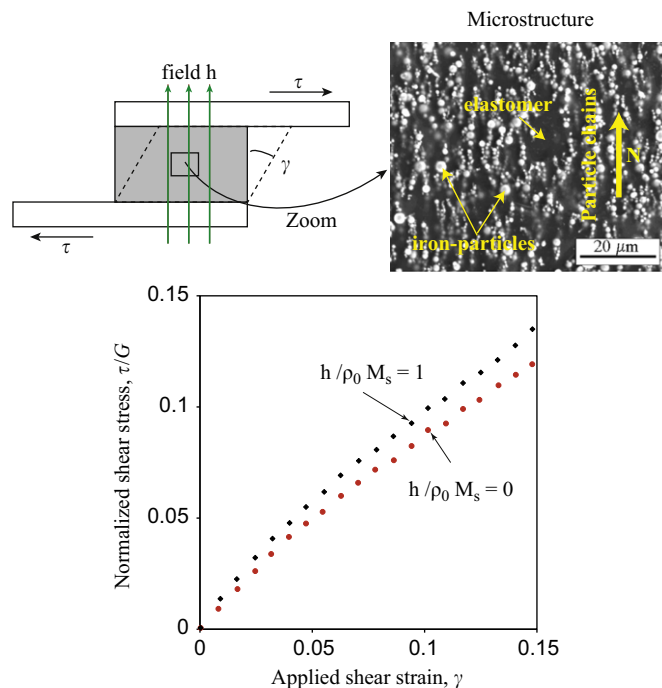


Fig. 1. Top left shows the schematics of a specimen subjected to simple shear in the presence of a magnetic field. Top right shows an electron micrograph (courtesy of Dr. John Ginder) of a MRE comprising 25% of iron particles of sizes ranging from 0.5 μm to 5 μm cured in a magnetic field. The application of a magnetic field during the curing process leads to formation of particle chains aligned with the curing field direction. In the bottom figure are experimental results showing the influence of the magnetic field on the MRE's simple shear response.

variational approaches result in the same set of governing equations. At the heart of this theory is a free energy density that depends on the magnetization per unit mass \mathbf{M} of the material, in contrast to other recent variational formulations (e.g., Brigadnov and Dorfmann, 2003; Dorfmann and Ogden, 2003), where the magnetic field \mathbf{B} is taken as the independent variable (see also Kovetz, 2000). The reason for choosing the specific magnetization \mathbf{M} as an independent variable lies in the facts that (i) this quantity vanishes outside the material and (ii) is unconstrained, whereas the magnetic field \mathbf{B} is present in the entire space, both inside and outside the solid in question and must satisfy a divergence-free constraint.

In addition to the continuum-based approach, a number of micromechanically based studies have recently appeared on the same subject. Their purpose has been to provide mean field (i.e., homogenized) theories for the macroscopic behavior of MRE's using a wide variety of simplifying assumptions about the local strain and magnetization fields, e.g., Jolly et al. (1996), Yin et al. (2006) – for particles aligned in chains, Liu et al. (2006) – for inclusions in the dilute limit, Corcolle et al. (2008) using small strain Hashin–Shtrikman homogenization, Borcea and Bruno (2001) – who use a dipole model as a fundamental building block for a small strain homogenized MRE model. Due to technical difficulties associated with large kinematics, the previously mentioned micromechanically based studies are in the small strain context, save for the recent work by Ponte Castañeda and Galipeau (2011).

The present work uses the theoretical formulation proposed by Kankanala and Triantafyllidis (2004) to determine the constitutive model for some recent MRE experiments. The composites in question are manufactured in the presence of a curing magnetic field and their iron particles form chain-like structures, thus requiring an anisotropic formulation of the energy density. Following this introduction, the description of the experiments is given in Section 2. The continuum model used for the experiments is presented in Section 3 and the work concludes with a discussion in Section 4. The micromechanical justification of the nonlinear mechanical response of the MRE at small strains is presented in Appendix A.

2. Experiments

2.1. Sample preparation and description

The MREs used in this study are similar to the ones used and described by Ginder et al. (1999). A brief description is hereby provided for the sake of completeness, but the interested reader is referred for a more detailed account to Kankanala (2007). The MREs consist of nearly spherical carbonyl iron particles (ISP, grade S-3700) embedded in natural rubber, i.e., *cis*-polyisoprene. The particle sizes range from approximately 0.5 μm to 5 μm and have a volume fraction of 25%. With the aid of the necessary crosslinkers and processing materials, these materials are mixed together on a typical two-roll mill. The resulting mixture is compression molded into disks in a mold specially designed with a wire coil which acts as the source of a 0.8 T magnetic field that is applied to the material during the curing process at a temperature of roughly 150 °C for approximately 15 min.

MRE samples are molded in disks of 60 mm in diameter by 2 mm and 10 mm thicknesses with the applied field during curing normal to the ends of the disks. Cylindrical samples (4.5 mm radius) for the magnetostriction tests described below are obtained from the 10 mm thick disks using standard water jet cutting technology. To assess anisotropic effects due to the chain-like structure of the particles, one set of samples is obtained with the cylinder axis normal to the ends of the disks (i.e., particle chain orientation parallel to cylinder axis and henceforth referred to as “*parallel sample*” when necessary) and the other set with the cylinder axis parallel to the ends of the disks (i.e., particle chain orientation perpendicular to the cylinder axis and henceforth referred to as “*perpendicular sample*” when necessary). Samples needed for the simple shear tests are manually cut out from the 2 mm thick disks into desired specimen sizes.

2.2. Magnetization and magnetostriction

A special dilatometer (see Fig. 2, designed by Ginder et al., 2002) is used to measure the strains in the cylindrical MREs induced by an externally applied magnetic field. The sample is in contact with the polished lower arm so that a length change in the specimen results in rotation of the lever about the low-friction sapphire bearings. At the free end of the lever, a capacitance sensor (Micro-Epsilon Capa NCDT Series 600) is fixed to the lower part of the fixture. As described in the product manual, the capacitance distance measurement is based on the principle of a parallel plate capacitor. When a constant AC current flows through the sensor capacitor, the amplitude of the AC voltage at the sensor is proportional to the distance between the capacitor electrodes. In this regard, the two plate electrodes are formed by the sensor and the (electrically conducting) lever arm. The capacitance sensor is calibrated so that a relation between voltage change (1 V) and the displacement of the lever arm is known (0.1 mm). Given the dimensions of the fixture, the length change in the specimen due to a known displacement at the end of the lever arm is calculated based on simple geometry. The magnetic field generated by the electromagnet (GMW 5403) is cycled, starting from zero to a maximum value then to a minimum value and finally back to zero. To ensure reasonable levels of repeatability, data were obtained for at least two cycles. The applied field near (i.e., < 1 mm from the sample boundary) the MRE specimen is measured using a Hall-effect Gaussmeter (Lakeshore 450). On account of the continuity in the tangential component of the field \mathbf{h} at the boundary, this measured value parallel to the sample component of \mathbf{h} just outside the sample may be taken to be the corresponding value just inside

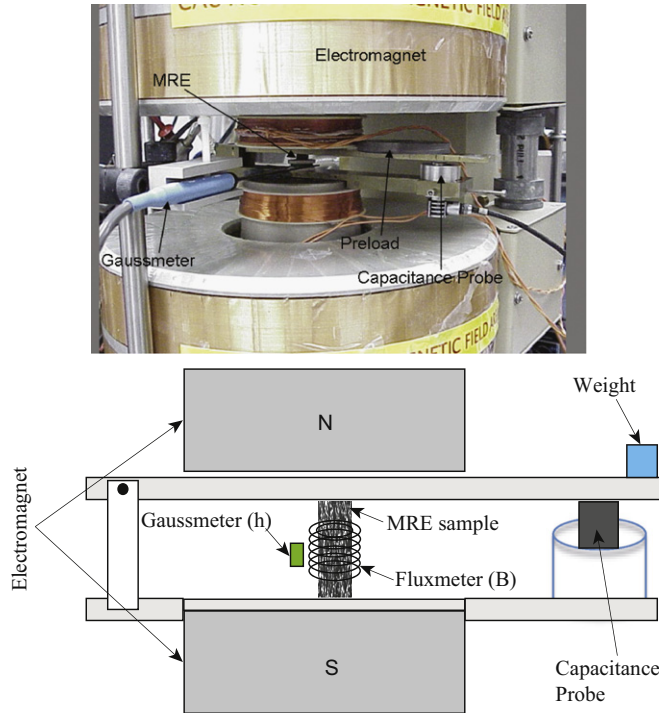


Fig. 2. Experimental setup to measure the magnetization and magnetostriction of an MRE for different uniaxial preloads.

the sample (assuming a uniform \mathbf{h} throughout the volume of the material). A coil concentric with the specimen is used to infer the magnetic field in the specimen.

Compressive preloads are applied to the sample by placing weights on the lever-arm. Tensile preloads are applied by first affixing the bottom end of the sample to the lower part of the fixture and the top end to the lever-arm using a cyanoacrylate adhesive. A mechanical spring (e.g., McMaster-Carr “394-11”, 0.4 gm, 16 mm, with a known force-displacement relationship) is then placed between the lever-arm and the lower part of the fixture. The compressed spring pushes against the lever arm which manifests as a tensile preload on the specimen. Note that the compression in the spring with initial length ≈ 8.5 mm is an order of magnitude less than the length change (≈ 0.05 mm) in the specimen. Hence, the change in the tensile preload, due to the change in the spring compression as the lever arm accommodates the specimen's length change, is small ($\leq 10\%$) and can be justifiably taken to be approximately constant.

As a consequence of the microstructure shown in Fig. 1, the MRE composite exhibits transversely isotropic symmetry with respect to the particle chain orientation vector \mathbf{N} . Moreover, the MRE has a longitudinal shear modulus $G = 1.0374$ MPa associated with the loading shown in Fig. 1, where the shearing direction is normal to the particle chains, and a magnetization saturation value $\mu_0 \rho_0 M_s \cong 0.45$ T with μ_0 denoting the magnetic permeability in vacuum, ρ_0 the initial density of the MRE and M_s the saturation magnetization of the MRE.

The nondimensional magnetization M/M_s in response to the nondimensional magnetic field $h/\rho_0 M_s$ applied parallel to the particle chains ($\mathbf{h} \parallel \mathbf{N}$) is shown in Fig. 3a. The response is obtained for the conditions of (i) zero external traction ($\sigma/G = 0$), (ii) compressive ($\sigma/G < 0$) and (iii) tensile ($\sigma/G > 0$) preloads. The response is linear in the nondimensional applied field range of $|h/\rho_0 M_s| \leq 0.3$ (approximately) with a magnetic susceptibility of $\chi_m = m/h = 0.5$ or a magnetic permeability, $\mu_r = B/h = \mu_0(1 + m/h) \cong 1.5\mu_0$. Saturation in magnetization occurs for nondimensional magnetic fields of $h/\rho_0 M_s \approx 1$. The saturation value is reasonable since $\mu_0 \rho_0 M_s = 2$ T for Fe and $\mu_0 \rho_0 M_s \cong 0.45$ T for the MRE composite while the volume fraction of the iron particles in the MRE is 25%, as indicated earlier. For dimensionless external prestresses in the range of $-0.192 \leq \sigma/G \leq 0.192$, we observe only a negligible change in the magnetization response. It is also worth noting that there is no indication of hysteresis in the $M-h$ response.

To evaluate the degree of magnetic anisotropy of the chosen MRE, the nondimensional magnetization response of a perpendicular sample ($\mathbf{h} \perp \mathbf{N}$) is compared with the response obtained from the parallel sample in Fig. 3b. It is readily seen that the magnetic susceptibility, χ_m , drops to 0.1 (or $\mu_r = 1.1$) for the perpendicular sample from $\chi_m = 0.5$ (or $\mu_r = 1.5$) for the parallel sample. As expected, the saturation of magnetization, which is a material constant, is independent of the particle chain orientation.

Therefore, two main observations can be made from these experiments: first, the magnetization response is practically insensitive to the applied prestress, which means that the stress-induced change of interparticle distances has a negligible effect on the average magnetization of the material. Second, the magnetization response is sensitive to particle chain

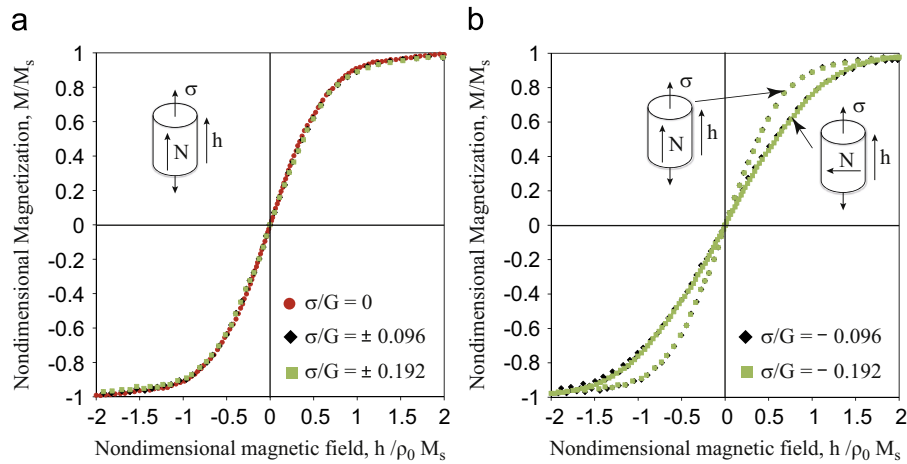


Fig. 3. Experimental measurements of the nondimensional magnetization M/M_s versus applied nondimensional magnetic field $h/\rho_0 M_s$ for a cylindrical MRE specimen under different dimensionless external prestresses σ/G . In part (a), the applied magnetic field is aligned with the particle chains ($\mathbf{h} \parallel \mathbf{N}$) and the applied traction direction. In part (b), results are shown for the case where the particle chains are either parallel ($\mathbf{h} \parallel \mathbf{N}$) or perpendicular ($\mathbf{h} \perp \mathbf{N}$) to the applied magnetic field.

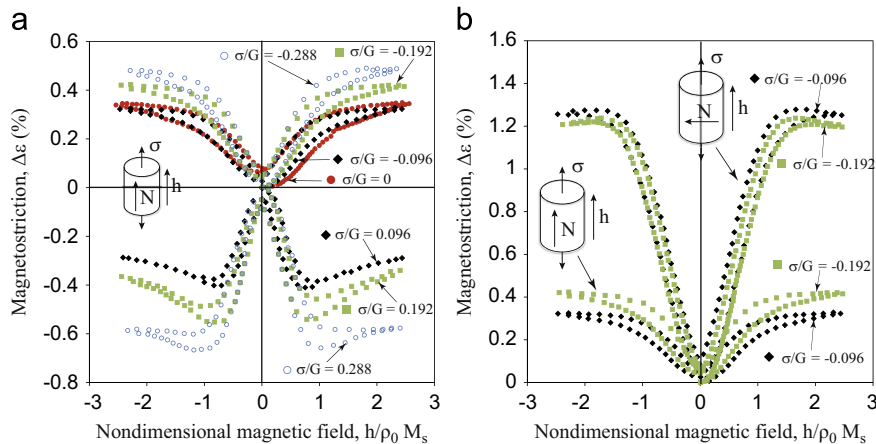


Fig. 4. Experimental measurements of the engineering strain change $\Delta\varepsilon$ versus the applied nondimensional magnetic field $h/\rho_0 M_s$ due to magnetostriction of a cylindrical MRE specimen subjected to different dimensionless external prestresses σ/G . In part (a), the applied magnetic field is parallel to both the particle chains ($\mathbf{h} \parallel \mathbf{N}$) and the applied traction direction. In part (b), the effect of the magnetic field orientation of $h/\rho_0 M_s$ with respect to the particle chains ($\mathbf{h} \parallel \mathbf{N}$ vs. $\mathbf{h} \perp \mathbf{N}$) is shown.

orientation with respect to the direction of the applied magnetic field and especially in the initial, linear range of this response. The decrease of the initial $M-h$ slope from the parallel to the perpendicular case is attributed to the different microgeometric particle arrangements which result in different macroscopic magnetization responses. It is also worth noticing that when the Fe particles reach magnetic saturation, the corresponding microgeometry differences for the two chain orientations, relatively to the applied magnetic field, are insignificant to the overall saturation magnetization.

The magnetostriction strain $\Delta\varepsilon$ versus the applied nondimensional magnetic field $h/\rho_0 M_s$ is shown in Fig. 4. In Fig. 4a, the magnetostriction is plotted for different preloads σ/G , which are aligned with the applied magnetic field and the particle chain ($\mathbf{h} \parallel \mathbf{N}$). In general, the magnitude of magnetostriction increases with the magnitude of the nondimensional preloads. Elongation strains increase from 0.34% for $\sigma/G = 0$ to about 0.48% for $\sigma/G = -0.288$. By comparison, the strains in the MREs are about double those seen in a magnetostrictive material like Terfenol-D (from 0.15% to 0.2%, Moffett et al., 1991). Negative strains are seen for all tensile prestresses with saturation strains of about 0.6% for $\sigma/G = +0.288$. Although a small amount of hysteresis is present in these experiments, especially near saturation levels, it is ignored in the subsequent modeling.

Interestingly, the magnetostriction response is not symmetric with respect to the sign of the prestress in Fig. 4a. Notice that the sample expands ($\Delta\varepsilon > 0$) for zero or negative prestresses ($-0.288 \leq \sigma/G \leq 0$) and contracts ($\Delta\varepsilon < 0$) for adequately large tensile prestresses ($0.096 \leq \sigma/G \leq 0.288$). This implies a strong nonlinear effect of the applied prestress on the resulting magnetostriction, which is directly attributed to the purely mechanical response of the MRE. More specifically,

due to the anisotropy of the MRE induced by the particle chains, a significant tension–compression asymmetry is present even at relatively small macroscopic strains ($\approx 2\text{--}5\%$). In this regard, the constitutive relation between prestrains and prestresses is nonlinear even at strains in the order of $\approx 2\text{--}5\%$, which suggests that the range of validity of small-strain approximations diminishes significantly in the case of initially anisotropic MREs of the type considered here. A prototypical mechanical model problem is proposed in the Appendix in order to show the effect of the microstructure on the overall stress–strain response of the MRE, particularly the resulting tension–compression asymmetry at relatively small macroscopic strains.

In addition to the tension–compression asymmetry of the magnetostrictive experiments in Fig. 4a, one can distinguish an initial quadratic range of the $\Delta\varepsilon\text{--}h$ response, expected at small strains and magnetic fields, followed by a saturation range at larger magnetic fields. The saturation strain levels are also influenced by prestress with strongest influence appearing for tensile prestresses. More specifically, we observe that while for zero or negative prestress the $\Delta\varepsilon\text{--}h$ response is monotonic, for adequately large positive prestresses the $\Delta\varepsilon\text{--}h$ response goes through a strain maximum before reaching a saturation level.

In Fig. 4b, we investigate the influence of particle chain orientation with respect to the applied magnetic field for two different compressive preloads. Notice that the initial curvature of the $\Delta\varepsilon\text{--}h$ response increases significantly for the case of particle chain orientation perpendicular to the applied magnetic field ($\mathbf{h} \perp \mathbf{N}$), as also do the corresponding saturation strains which are three to four times larger (depending on prestress) than those corresponding to the parallel case ($\mathbf{h} \parallel \mathbf{N}$).

Motivated by these observations for both the parallel and perpendicular samples and particularly by the counter-intuitive results for the magnetostriction (e.g., $\Delta\varepsilon > 0$ for no prestress), the authors propose a deformation mechanism, sketched in Fig. 5, which could explain the previously observed responses. The proposed local deformation mechanism to

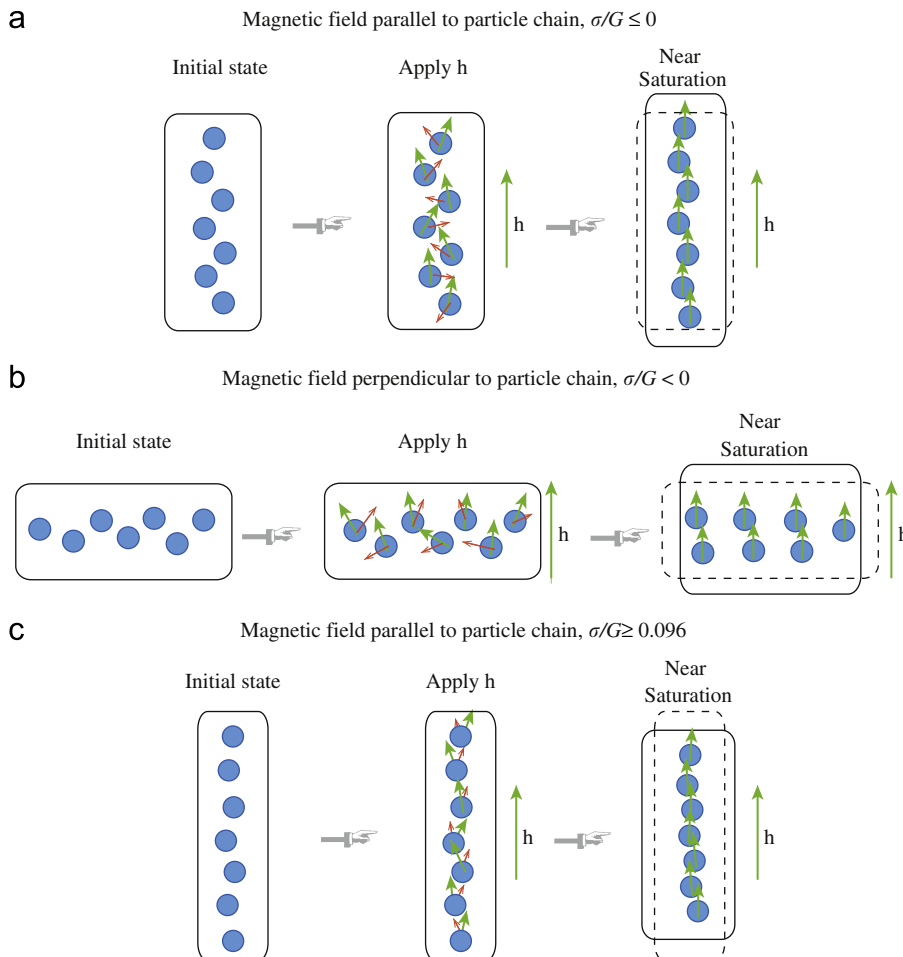


Fig. 5. Mechanism of deformation upon application of external magnetic field in a direction parallel and perpendicular to the particle chains and different prestresses σ/G . The direction of the large (green-color) arrows indicates the direction of effective magnetic dipoles, i.e., from south to north pole. The small (red-color) arrows indicate the direction of motion of the particle due to the magnetic forces. (a) Magnetic field parallel to particle chain, $\sigma/G \leq 0$. (b) Magnetic field perpendicular to particle chain, $\sigma/G < 0$. (c) Magnetic field parallel to particle chain, $\sigma/G \geq 0.096$. (For interpretation of the references to color in this figure legend, the reader is referred to the web version of this article.)

be detailed in the following has its roots in the original work of [Klingenberg and Zukoski \(1990\)](#) (in the context of electrorheological suspensions) and [Lemaire and Bossis \(1991\)](#) and [Bossis and Lemaire \(1991\)](#) (in the context of magnetic suspensions), who found that between a pair of particles subjected to a magnetic (or electric) field, there exists a *restoring force* which is, in general, non-aligned to the applied magnetic (or electric) field and tends to align the particles with the applied magnetic (or electric) field so that they form magnetic (or electric) dipoles. Similar observations have also been made in the more recent work of [Borcea and Bruno \(2001\)](#) in the context of two-particle magnetostatic systems at small strain.

As sketched in [Fig. 5a](#) for $\sigma/G \leq 0$, the particles are taken to be somewhat aligned in a staggered configuration. However, it is important that we do not allow for a perfect alignment of the particles in accord with the electron micrograph shown in [Fig. 1](#). Then, by application of the field \mathbf{h} parallel to the particle chain, the particles become magnetic dipoles with effective magnetization direction indicated by the large (green-color) arrows that tend to align themselves with the externally applied magnetic field. The optimal configuration would be the one that the south magnetic pole of a particle on top approaches the north magnetic pole of the particle below. In order to achieve such a configuration, the particles must move in a direction almost perpendicular to \mathbf{h} , as indicated by the small (red-color) arrows in [Fig. 5a](#). This interparticle motion leads to a contraction in the direction normal to \mathbf{h} and consequently due to matrix incompressibility to an overall extension of the MRE along \mathbf{h} .

The mechanism remains exactly the same in the case of the perpendicular sample with $\sigma/G < 0$, as shown in [Fig. 5b](#). In fact, in the perpendicular sample, due to the presence of magnetic dipoles with the same directionality as well as the small interparticle distance normal to the externally applied magnetic field, the repulsive forces of the neighboring particles are even stronger than in the parallel case. This induces a much more significant motion of the particles in the direction normal to the applied field \mathbf{h} . This is done in order to finally reach a state where pairs of particles are created forming pair-magnetic dipoles in the direction of the applied field \mathbf{h} , while at the same time increasing the distance between two such neighboring dipoles. This results again in a contraction normal to the applied magnetic field and hence due to matrix incompressibility in an extension parallel to \mathbf{h} . Only this extension is larger in the perpendicular sample than in the parallel one since the particles are forced to move more in order to form these pair-magnetic dipoles. Consequently, one obtains a larger magnetostriction for the perpendicular sample than for the parallel one, which is in

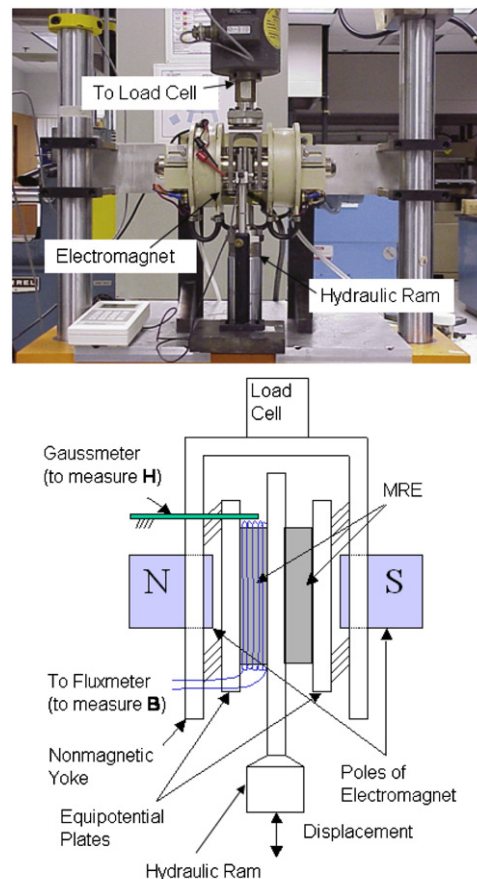


Fig. 6. Experimental setup for measuring the simple shear response of an MRE under different magnetic fields.

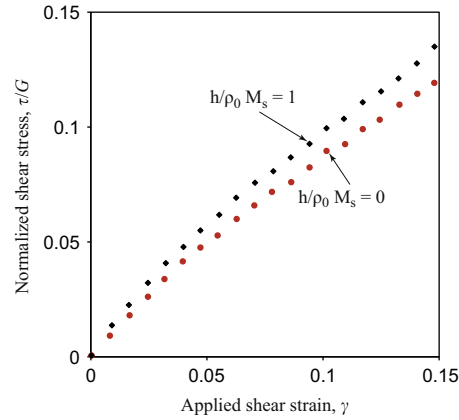


Fig. 7. Experimental shear stress–strain results in the absence or in the presence of a magnetic field. The particle chains are initially parallel to the applied nondimensional magnetic field $h/\rho_0 M_s$ and perpendicular to the shearing direction.

accord with the experimental results in Fig. 4b. We should also mention that the previously proposed deformation mechanism is also present in isotropic MREs, where positive magnetostrictions have been observed for no-prestress samples (Diguët et al., 2010).

By contrast, if adequately large positive prestresses (e.g., $\sigma/G \geq 0.096$) are applied then the interparticle distance increases and attractive forces between particles appear now in the direction of the applied magnetic field, leading to an overall compressive magnetostriction, as shown in Fig. 5c. However, as we observe here it is necessary that the particles are significantly far apart in order to result in an overall negative magnetostrictive response for the MRE.

2.3. Simple shear

The simple shear response of the MRE specimens is obtained by cutting out two rectangular slabs of dimensions $24 \text{ mm} \times 12 \text{ mm} \times 2 \text{ mm}$ from the elastomer disks mentioned in Section 2.1 and bonding each sample, using a cyanoacrylate adhesive, between the equipotential plate on one side and the “tongue” of the double-lap shear fixture on the other side, as shown in Fig. 6.² The double-lap fixture is attached to a conventional servohydraulic testing machine (Instron model 1331). The shear stresses are applied in a plane perpendicular to the direction of the particle chain orientation, the latter being parallel to the direction of the applied magnetic field. The external magnetic field is generated by a C-frame electromagnet (GMW 3470) mounted around the double-lap fixture, as shown in Fig. 6. An operational amplifier power supply (Kepco BOP 50-8) is used to drive the electromagnet. The average flux density in the MRE sample is found by using a sense coil wound (10 turns) around the circumference of the sample and integrating the voltage induced in the coils using a fluxmeter (Walker Scientific, model MF-3D). The field \mathbf{h} in the gap between the equipotential plates (see Fig. 6) close to the specimen (i.e., $\approx 1 \text{ mm}$ from the side) is measured using a Hall-effect Gaussmeter (Lakeshore 450).

The experimentally observed response of the MRE when subjected to simple shear loading in the absence or in the presence of a magnetic field parallel to the particle chain orientation is shown in Fig. 7. Notice that the initial longitudinal shear modulus G appears to be rather insensitive to the presence of a strong magnetic field, while the material becomes stiffer under the presence of a magnetic field once shear strain increases. It should be pointed out here that the magnetic field effect on the material’s simple shear response is much less pronounced (of the order of 10% for $\gamma = 0.15$) than in the previously discussed cases of magnetostriction. This indicates that if maximum magnetoelastic coupling effects are required in application, shearing is the least effective method to achieve them.

3. Modeling

In this section, we review first the constitutive laws and boundary conditions for magnetoelastic continua. For a detailed derivation of the governing equations, the reader is referred to the work of Kankanala and Triantafyllidis (2004), and the references therein. Unless otherwise indicated, all the required field quantities are defined in the current configuration. We use standard notation with bold letters representing tensors and normal script scalars. In what follows, general constitutive laws are presented first. Next, the constitutive response of the MRE at small magnetic fields is analyzed followed by the discussion of the MRE constitutive response at large magnetic fields. Finally, the quasiconvexity of the proposed energy density is discussed.

² The test procedure generally utilizes the methods used previously by Ginder et al. (1999) in dynamic simple shear testing.

3.1. Free energy and general constitutive laws

Of interest here is the determination of the specific free energy $\hat{\psi}$ that best fits the MRE experiments. The general form of the specific Helmholtz free energy (i.e., per unit mass) is given by

$$\hat{\psi} = \hat{\psi}(\mathbf{C}, \mathbf{M}), \quad \mathbf{C} = \mathbf{F}^T \bullet \mathbf{F}, \quad (1)$$

where \mathbf{F} is the material's deformation gradient (\mathbf{F}^T denotes its transpose), \mathbf{C} denotes the right "Cauchy–Green" tensor and \mathbf{M} the specific magnetization. Following Kankanala and Triantafyllidis (2004) (c.f. relations (2.42) and (2.44) in that reference), we have the following expression for the total Cauchy stress $\boldsymbol{\sigma}$:

$$\boldsymbol{\sigma} = \rho \left[2\mathbf{F} \bullet \frac{\partial \hat{\psi}}{\partial \mathbf{C}} \bullet \mathbf{F}^T + \mu_0(\mathbf{M}\mathbf{h} + \mathbf{h}\mathbf{M}) \right] + \mu_0 \left[\mathbf{h}\mathbf{h} - \frac{1}{2}(\mathbf{h} \bullet \mathbf{h})\mathbf{I} \right]. \quad (2)$$

Here, ρ is the current material density, while it is noted that in vacuum (i.e., $\rho = 0$), the total stress is non-zero and equals the Maxwell stress $\mu_0[\mathbf{h}\mathbf{h} - (1/2)(\mathbf{h} \bullet \mathbf{h})\mathbf{I}]$. In addition, the field \mathbf{h} is given by

$$\mu_0 \mathbf{h} = \frac{\partial \hat{\psi}}{\partial \mathbf{M}}. \quad (3)$$

The surface tractions \mathbf{t} can be readily obtained from (2) (see (2.48) in Kankanala and Triantafyllidis, 2004) by

$$\mathbf{t} = \rho \left[2\mathbf{F} \bullet \frac{\partial \hat{\psi}}{\partial \mathbf{C}} \bullet \mathbf{F}^T + \mu_0 \mathbf{M}\mathbf{h} - \frac{\rho \mu_0}{2}(\mathbf{M} \bullet \mathbf{n})^2 \mathbf{I} \right] \bullet \mathbf{n}, \quad (4)$$

with \mathbf{n} denoting the unit normal to the surface under consideration.

As already pointed out in Section 2, the material under investigation is a transversely isotropic composite since the iron particles form chains along a certain direction. This implies that the free energy function $\hat{\psi}$ should also depend on the unit vector \mathbf{N} (see Fig. 1), which defines the initial orientation of the particle chains. Thus,

$$\hat{\psi} = \hat{\psi}(\mathbf{C}, \mathbf{N}, \mathbf{M}), \quad \mathbf{N} \bullet \mathbf{N} = 1. \quad (5)$$

Using the general theory of transversely isotropic functions (Adkins, 1959, 1960; Pipkin and Rivlin, 1959) that depend on a rank-two tensor, the right Cauchy–Green tensor \mathbf{C} , and two vectors, the orientation vector \mathbf{N} and the magnetization \mathbf{M} , one obtains that $\hat{\psi}$ is a function of ten independent invariants, namely

$$\begin{aligned} I_1 &= \text{tr } \mathbf{C}, & I_2 &= \frac{1}{2}[(\text{tr } \mathbf{C})^2 - \text{tr } \mathbf{C}^2], & I_3 &= \det \mathbf{C}, \\ I_4 &= \mathbf{N} \bullet \mathbf{C} \bullet \mathbf{N}, & I_5 &= \mathbf{N} \bullet \mathbf{C}^2 \bullet \mathbf{N}, \\ I_6 &= \mathbf{M} \bullet \mathbf{M}, & I_7 &= \mathbf{M} \bullet \mathbf{C} \bullet \mathbf{M}, & I_8 &= \mathbf{M} \bullet \mathbf{C}^2 \bullet \mathbf{M}, \\ I_9 &= (\mathbf{M} \bullet \mathbf{N})^2, & I_{10} &= (\mathbf{M} \bullet \mathbf{N})(\mathbf{M} \bullet \mathbf{C} \bullet \mathbf{N}). \end{aligned} \quad (6)$$

The elastomeric composite under investigation is nearly incompressible, hence use is made of the incompressibility condition, $\det \mathbf{F} = \det \mathbf{C} = 1$, which implies that the free energy function is independent of I_3 , while the current material density ρ equals the initial one ρ_0 , i.e., $\rho = \rho_0$. Moreover, motivated by recent results on fiber reinforced polymers (e.g., deBotton et al., 2006), we also make the hypothesis that the energy function does not depend on I_2 and I_5 . For additional simplicity, we also assume that the energy function depends on the invariants in an additive manner, allowing us to use a free energy function of the form:

$$\rho_0 \hat{\psi} = \Psi(I_1, I_4, I_6, I_7, I_8, I_9, I_{10}) = \sum_{\substack{K=1 \\ K \neq 2,3,5}}^{10} \Psi_K(I_K). \quad (7)$$

Consequently, Eqs. (3) and (4) for the field \mathbf{h} and traction \mathbf{t} , respectively, are given by

$$\rho_0 \mu_0 \mathbf{h} = \sum_{K=6}^{10} \frac{\partial \Psi}{\partial I_K} \frac{\partial I_K}{\partial \mathbf{M}} \quad (8)$$

and

$$\mathbf{t} = \left[2\mathbf{F} \bullet \sum_{\substack{K=1 \\ K \neq 2,3,5}}^{10} \frac{\partial \Psi}{\partial I_K} \frac{\partial I_K}{\partial \mathbf{C}} \bullet \mathbf{F}^T + \mu_0 \rho_0 \mathbf{M}\mathbf{h} + \left(p - \frac{\mu_0}{2}(\rho_0 \mathbf{M} \bullet \mathbf{n})^2 \right) \mathbf{I} \right] \bullet \mathbf{n}, \quad (9)$$

where the terms $\partial I_K / \partial \mathbf{C}$ and $\partial I_K / \partial \mathbf{M}$ are obtained from (6). In expression (9), p is the Lagrange multiplier associated with the constraint of incompressibility $I_3 = 1$ and denotes the pressure, which is evaluated from the lateral traction boundary conditions of the specimen.

3.2. Constitutive response for small magnetic fields

Finding an energy density Ψ that best fits the experiments reported in Section 2 is done in two steps: first an energy density function is sought that describes the experiments for relatively small magnetic fields, since for $|h/\rho_0 M_s| < 0.3$ the $M-h$ response is essentially linear and the $\Delta\varepsilon-h$ response essentially quadratic. For this case only a handful of constants are fitted to selected tests. The resulting energy density shows excellent agreement with all available test data for small magnetic fields. The second step pertains to finding an energy density function valid for large magnetization, a task detailed in the next subsection.

The experiments presented in the previous section involve three different setups; (a) uniaxial stress tests in the direction of a magnetic field which is aligned with the particle chains, (b) uniaxial stress tests in the direction of a magnetic field which is perpendicular to the particle chains and (c) simple shear tests where the particle chains are initially aligned with the applied magnetic field.

3.2.1. Uniaxial stress tests with magnetic field aligned with particle chains

In these tests, the MRE specimen is a cylinder with its symmetry axis along the \mathbf{e}_1 direction, which is also the initial particle chains orientation. The specimen is subjected to uniaxial prestressing \mathbf{t} and a uniform field \mathbf{h} , both in the direction of the cylinder axis, such that $\mathbf{h} \parallel \mathbf{N}$. Denoting by λ the stretch ratio along the axial direction \mathbf{e}_1 and considering the material's incompressibility and transverse isotropy, the right Cauchy–Green tensor \mathbf{C} , the particle chain orientation \mathbf{N} , the field \mathbf{h} and the magnetization per unit mass \mathbf{M} take the form:

$$\mathbf{C} = \lambda^2 \mathbf{e}_1 \mathbf{e}_1 + \frac{1}{\lambda} (\mathbf{e}_2 \mathbf{e}_2 + \mathbf{e}_3 \mathbf{e}_3), \quad \mathbf{N} = \mathbf{e}_1, \quad \mathbf{h} = h \mathbf{e}_1, \quad \mathbf{M} = M \mathbf{e}_1. \quad (10)$$

Making use of (10), we obtain the following relation between $M-h$ from (8), i.e.,

$$\rho_0 \mu_0 h = 2M \left[\frac{\partial \Psi}{\partial I_6} + \lambda^2 \frac{\partial \Psi}{\partial I_7} + \lambda^4 \frac{\partial \Psi}{\partial I_8} + \frac{\partial \Psi}{\partial I_9} + \lambda^2 \frac{\partial \Psi}{\partial I_{10}} \right], \quad (11)$$

whereas the axial traction, defined in (9), $\mathbf{t} = \sigma \mathbf{e}_1$ at the end section with normal $\mathbf{n} = \mathbf{e}_1$ becomes

$$\sigma = 2 \left[\frac{\partial \Psi}{\partial I_1} \left(\lambda^2 - \frac{1}{\lambda} \right) + \frac{\partial \Psi}{\partial I_4} \lambda^2 + M^2 \left(\frac{\partial \Psi}{\partial I_7} \lambda^2 + 2 \frac{\partial \Psi}{\partial I_8} \lambda^4 + \frac{\partial \Psi}{\partial I_{10}} \lambda^2 \right) \right] + \mu_0 \rho_0 M \left[h - \frac{\rho_0 M}{2} \right]. \quad (12)$$

In the above expression use has been made of the result for the scalar pressure

$$p = -\frac{2}{\lambda} \frac{\partial \Psi}{\partial I_1}, \quad (13)$$

obtained from the requirement that the lateral tractions $\mathbf{t} = \mathbf{0}$ for $\mathbf{n} = \mathbf{e}_2$ (or equivalently $\mathbf{n} = \mathbf{e}_3$ due to transverse isotropy and axisymmetry in this case).

Recall that the experimental results show that the overall magnetostriction obtained is small, i.e., $|\Delta\varepsilon| \ll 1$. On the other hand, the applied prestress σ/G (with G denoting the longitudinal shear modulus of the MRE) has a significant nonlinear effect on the magnetostriction results, as discussed in the context of Fig. 4a. Consequently the influence of the resulting prestretch, denoted as λ_0 in the direction \mathbf{e}_1 (and hence $1/\sqrt{\lambda_0}$ in the directions \mathbf{e}_2 and \mathbf{e}_3 , respectively due to incompressibility), is not negligible leading to the following expressions for the stretch ratio along \mathbf{e}_1

$$\lambda = \lambda_0 [1 + \Delta\varepsilon + \mathcal{O}(\Delta\varepsilon^2)]. \quad (14)$$

By substituting (14) in Eqs. (11) and (12) and by consideration of only first order terms in $\Delta\varepsilon$, we obtain the expressions for the initial slope of the $M-h$ response:

$$\left. \frac{\partial M}{\partial h} \right|_{\Delta\varepsilon=0, M=0} = \frac{\mu_0 \rho_0}{2} \left[\frac{\partial \Psi}{\partial I_6} + \lambda_0^2 \frac{\partial \Psi}{\partial I_7} + \lambda_0^4 \frac{\partial \Psi}{\partial I_8} + \frac{\partial \Psi}{\partial I_9} + \lambda_0^2 \frac{\partial \Psi}{\partial I_{10}} \right]^{-1}_{\Delta\varepsilon=0, M=0} \quad (15)$$

and the initial curvature of the $\Delta\varepsilon-h$ response

$$\left. \frac{\partial^2 \Delta\varepsilon}{\partial h^2} \right|_{\Delta\varepsilon=0, M=0} = \left\{ \left[\frac{\mu_0 \rho_0^2}{2} - 2 \left(\frac{\partial \Psi}{\partial I_6} + \frac{\partial \Psi}{\partial I_9} + 2 \lambda_0^2 \left(\frac{\partial \Psi}{\partial I_7} + \frac{\partial \Psi}{\partial I_{10}} \right) + 3 \lambda_0^4 \frac{\partial \Psi}{\partial I_8} \right) \right] \right. \\ \left. \times \left[\left(\frac{1}{\lambda_0} + 2 \lambda_0^2 \right) \frac{\partial \Psi}{\partial I_1} + 2 \lambda_0^2 \frac{\partial \Psi}{\partial I_4} + 2 \left(\lambda_0^2 - \frac{1}{\lambda_0} \right)^2 \frac{\partial^2 \Psi}{\partial I_1 \partial I_1} + 2 \lambda_0^4 \frac{\partial^2 \Psi}{\partial I_4 \partial I_4} \right]^{-1} \left(\frac{\partial M}{\partial h} \right)^2 \right\}_{\Delta\varepsilon=0, M=0}, \quad (16)$$

with $\partial M/\partial h$ given by (15).

In the above two expressions, the prestretch λ_0 is evaluated in terms of the applied prestress, σ , by considering the purely mechanical response (i.e., $\Delta\varepsilon = 0$ and $M = 0$) in (12), i.e., by the nonlinear algebraic equation:

$$\sigma = 2 \left[\left(\lambda_0^2 - \frac{1}{\lambda_0} \right) \frac{\partial \Psi}{\partial I_1} + \lambda_0^2 \frac{\partial \Psi}{\partial I_4} \right]_{\Delta\varepsilon=0, M=0}, \quad (17)$$

thus completing the governing equations for this test.

3.2.2. Uniaxial stress tests with magnetic field normal to particle chains

In these tests, the MRE specimen is a cylinder with its symmetry axis along the \mathbf{e}_1 direction, which is perpendicular to the initial particle chains orientation \mathbf{e}_2 . The specimen is subjected to uniaxial prestressing \mathbf{t} and a uniform field \mathbf{h} , both in the direction of the cylinder axis, such that $\mathbf{h} \perp \mathbf{N}$. Denoting by λ and $\bar{\lambda}$ the stretch ratios along the axial direction \mathbf{e}_1 and particle chain direction \mathbf{e}_2 , respectively, and considering the material's incompressibility, the right Cauchy–Green tensor \mathbf{C} , the particle chain orientation vector \mathbf{N} , the field \mathbf{h} and the magnetization per unit mass \mathbf{M} take the form

$$\mathbf{C} = \lambda^2 \mathbf{e}_1 \mathbf{e}_1 + \bar{\lambda}^2 \mathbf{e}_2 \mathbf{e}_2 + \frac{1}{\lambda^2 \bar{\lambda}^2} \mathbf{e}_3 \mathbf{e}_3, \quad \mathbf{N} = \mathbf{e}_2, \quad \mathbf{h} = h \mathbf{e}_1, \quad \mathbf{M} = M \mathbf{e}_1. \quad (18)$$

Making use of (18), we obtain the following relation between $M-h$ from (8):

$$\rho_0 \mu_0 h = 2M \left[\frac{\partial \Psi}{\partial I_6} + \lambda^2 \frac{\partial \Psi}{\partial I_7} + \lambda^4 \frac{\partial \Psi}{\partial I_8} \right]. \quad (19)$$

Note that in this case of $\mathbf{h} \perp \mathbf{N}$, I_9 and I_{10} vanish, since $\mathbf{N} \cdot \mathbf{M} = 0$.

The corresponding axial traction, defined in (9), $\mathbf{t} = \sigma \mathbf{e}_1$ at the end section with normal $\mathbf{n} = \mathbf{e}_1$ becomes

$$\sigma = 2 \left[\frac{\partial \Psi}{\partial I_1} \left(\lambda^2 - \frac{1}{\lambda^2 \bar{\lambda}^2} \right) + M^2 \lambda^2 \left(\frac{\partial \Psi}{\partial I_7} + 2 \lambda^2 \frac{\partial \Psi}{\partial I_8} \right) \right] + M \mu_0 \rho_0 \left(h - \frac{\rho_0 M}{2} \right). \quad (20)$$

Considering next the traction-free boundary conditions, $\mathbf{t} = \mathbf{0}$ for $\mathbf{n} = \mathbf{e}_2$ and $\mathbf{t} = \mathbf{0}$ for $\mathbf{n} = \mathbf{e}_3$, we obtain respectively two equations for the pressure p :

$$p = -\frac{2}{\lambda^2 \bar{\lambda}^2} \frac{\partial \Psi}{\partial I_1} = -2 \bar{\lambda}^2 \left(\frac{\partial \Psi}{\partial I_1} + \frac{\partial \Psi}{\partial I_4} \right). \quad (21)$$

The first of these equations has already been taken into account in (20), while the second will be used to solve for $\bar{\lambda}$.

We again use an expansion about small magnetostrictive strains $\Delta \varepsilon$ and $-\bar{\nu} \Delta \varepsilon$ but large prestretches λ_0 and $\bar{\lambda}_0$ along \mathbf{e}_1 and \mathbf{e}_2 (strains along \mathbf{e}_3 are found from incompressibility), such that

$$\lambda = \lambda_0 [1 + \Delta \varepsilon + \mathcal{O}(\Delta \varepsilon^2)], \quad \bar{\lambda} = \bar{\lambda}_0 [1 - \bar{\nu} \Delta \varepsilon + \mathcal{O}(\Delta \varepsilon^2)], \quad (22)$$

where $\bar{\nu}$ is the initial poisson ratio along \mathbf{e}_2 , to be determined later in this section.

By substituting (22) in Eqs. (19) and (20), we obtain the following expressions for the initial slope of the $M-h$ response:

$$\left. \frac{\partial M}{\partial h} \right|_{\Delta \varepsilon = 0, M = 0} = \frac{\rho_0 \mu_0}{2} \left[\frac{\partial \Psi}{\partial I_6} + \lambda_0^2 \frac{\partial \Psi}{\partial I_7} + \lambda_0^4 \frac{\partial \Psi}{\partial I_8} \right]^{-1}_{\Delta \varepsilon = 0, M = 0} \quad (23)$$

and the initial curvature of the $\Delta \varepsilon-h$ response

$$\begin{aligned} \left. \frac{\partial^2 \Delta \varepsilon}{\partial h^2} \right|_{\Delta \varepsilon = 0, M = 0} &= \left\{ \left[\frac{\mu_0 \rho_0^2}{2} - 2 \left(\frac{\partial \Psi}{\partial I_6} + 2 \lambda_0^2 \frac{\partial \Psi}{\partial I_7} + 3 \lambda_0^4 \frac{\partial \Psi}{\partial I_8} \right) \right] \right. \\ &\quad \times \left[2 \left(\lambda_0^2 + \frac{1 - \bar{\nu}}{\lambda_0^2 \bar{\lambda}_0^2} \right) \frac{\partial \Psi}{\partial I_1} + \left(\frac{2(\lambda_0^4 \bar{\lambda}_0^{-2} - 1)(-\bar{\nu} \lambda_0^2 \bar{\lambda}_0^4 + \bar{\nu} + \lambda_0^4 \bar{\lambda}_0^{-2} - 1)}{\lambda_0^4 \bar{\lambda}_0^4} \right) \frac{\partial^2 \Psi}{\partial I_1 \partial I_1} \right]^{-1} \left. \left(\frac{\partial M}{\partial h} \right)^2 \right\}_{\Delta \varepsilon = 0, M = 0}. \end{aligned} \quad (24)$$

In the above expressions, the prestretches λ_0 and $\bar{\lambda}_0$ are evaluated by considering the purely mechanical response (i.e., $\Delta \varepsilon = 0$ and $M = 0$) in (20) and (21), i.e., by solving the system of two coupled nonlinear algebraic equations

$$\sigma = 2 \left[\lambda_0^2 - \frac{1}{\lambda_0^2 \bar{\lambda}_0^2} \right] \frac{\partial \Psi}{\partial I_1} \Big|_{\Delta \varepsilon = 0, M = 0}, \quad \left[\frac{1}{\lambda_0^2 \bar{\lambda}_0^2} \frac{\partial \Psi}{\partial I_1} - \bar{\lambda}_0^2 \left(\frac{\partial \Psi}{\partial I_1} + \frac{\partial \Psi}{\partial I_4} \right) \right] \Big|_{\Delta \varepsilon = 0, M = 0} = 0. \quad (25)$$

By considering the $\mathcal{O}(\Delta \varepsilon)$ terms in the second equation of (21), one finds the poisson ratio, $\bar{\nu}$, along \mathbf{e}_2 to be

$$\begin{aligned} \bar{\nu} &= \left\{ \left[\lambda_0^2 \bar{\lambda}_0^2 \frac{\partial \Psi}{\partial I_1} + (\lambda_0^4 \bar{\lambda}_0^{-2} - 1)(\lambda_0^2 \bar{\lambda}_0^{-4} - 1) \frac{\partial^2 \Psi}{\partial I_1 \partial I_1} \right] \right. \\ &\quad \times \left. \left[\lambda_0^2 \bar{\lambda}_0^2 (\lambda_0^2 \bar{\lambda}_0^4 + 1) \frac{\partial \Psi}{\partial I_1} + \lambda_0^4 \bar{\lambda}_0^6 \frac{\partial \Psi}{\partial I_4} + (\lambda_0^2 \bar{\lambda}_0^{-4} - 1)^2 \frac{\partial^2 \Psi}{\partial I_1 \partial I_1} + \lambda_0^4 \bar{\lambda}_0^8 \frac{\partial^2 \Psi}{\partial I_4 \partial I_4} \right]^{-1} \right\}_{\Delta \varepsilon = 0, M = 0}, \end{aligned} \quad (26)$$

thus completing the set of equations for this test.

3.2.3. Simple shear tests subjected to a magnetic field along the initial particle chain direction

In the case of simple shear loading with strain γ , i.e., with $\mathbf{F} = \mathbf{I} + \gamma \mathbf{e}_1 \mathbf{e}_2$, where the reference particle chain direction and the applied magnetic field are aligned in the \mathbf{e}_1 direction, one has

$$\mathbf{C} = \mathbf{e}_1 \mathbf{e}_1 + \mathbf{e}_3 \mathbf{e}_3 + (1 + \gamma^2) \mathbf{e}_2 \mathbf{e}_2 + \gamma (\mathbf{e}_1 \mathbf{e}_2 + \mathbf{e}_2 \mathbf{e}_1), \quad \mathbf{N} = \mathbf{e}_1, \quad \mathbf{h} = (h - \rho_0 M) \mathbf{e}_1, \quad \mathbf{M} = M_1 \mathbf{e}_1 + M_2 \mathbf{e}_2. \quad (27)$$

In the above expressions, use has been made of the continuity of the component of the magnetic field $\mathbf{h} = \mu_0(\mathbf{h} + \rho_0\mathbf{M})$ along the \mathbf{e}_1 direction and the component of \mathbf{h} along the \mathbf{e}_2 direction.

Substitution of these expressions in (8) gives the component of the field \mathbf{h} in the \mathbf{e}_1 direction:

$$\mu\rho_0(h - \rho_0M_1) = 2\frac{\partial\Psi}{\partial I_6}M_1 + 2\frac{\partial\Psi}{\partial I_7}(M_1 + M_2\gamma) + 2\frac{\partial\Psi}{\partial I_9}M_1 + 2\frac{\partial\Psi}{\partial I_8}[M_1(1 + \gamma^2) + M_2\gamma(2 + \gamma^2)] + \frac{\partial\Psi}{\partial I_{10}}(2M_1 + M_2\gamma) \quad (28)$$

and the component of the field \mathbf{h} in the \mathbf{e}_2 direction

$$0 = 2\frac{\partial\Psi}{\partial I_6}M_2 + 2\frac{\partial\Psi}{\partial I_7}[M_1\gamma + M_2(\gamma^2 + 1)] + 2\frac{\partial\Psi}{\partial I_8}[M_1\gamma(\gamma^2 + 2) + M_2(\gamma^4 + 3\gamma^2 + 1)] + \frac{\partial\Psi}{\partial I_{10}}M_1\gamma. \quad (29)$$

The traction (defined in (9)) on the face with normal $\mathbf{n} = \mathbf{e}_1$ is $\mathbf{t} = \sigma\mathbf{e}_1 + \tau\mathbf{e}_2$, where the shear stress τ is given by

$$\tau = 2\gamma\frac{\partial\Psi}{\partial I_1} + \frac{\partial\Psi}{\partial I_7}(2M_1M_2 + 2M_2^2\gamma) + \frac{\partial\Psi}{\partial I_{10}}M_1M_2 + 2\frac{\partial\Psi}{\partial I_8}[M_1^2\gamma + M_1M_2(3\gamma^2 + 2) + M_2^2\gamma(2\gamma^2 + 3)] + \mu_0\rho_0(h - \rho_0M_1)M_2, \quad (30)$$

thus completing the set of equations for the shear tests for large shear strains γ .

Specializing the above expressions for small shear strains, i.e., expanding about $\gamma = 0$ and keeping only $\mathcal{O}(\gamma)$ terms, one obtains from (29) the following relation between M_2 and M_1 :

$$M_2 = -M_1 \left\{ \left[\frac{\partial\Psi}{\partial I_7} + 2\frac{\partial\Psi}{\partial I_8} + \frac{1}{2}\frac{\partial\Psi}{\partial I_{10}} \right] \left[\frac{\partial\Psi}{\partial I_6} + \frac{\partial\Psi}{\partial I_7} + \frac{\partial\Psi}{\partial I_8} \right]^{-1} \right\}_{\gamma=0} \gamma + \mathcal{O}(\gamma^2), \quad (31)$$

while, the initial shear stress–strain slope becomes

$$\begin{aligned} \left. \frac{\partial\tau}{\partial\gamma} \right|_{\gamma=0} &= 2\left. \frac{\partial\Psi}{\partial I_7} \right|_{\gamma=0} - M_1^2 \left\{ \left[\frac{\partial\Psi}{\partial I_6} + \frac{\partial\Psi}{\partial I_7} + \frac{\partial\Psi}{\partial I_8} \right]^{-1} \left[\frac{\partial\Psi}{\partial I_{10}} \left(5\frac{\partial\Psi}{\partial I_7} + 9\frac{\partial\Psi}{\partial I_8} + \frac{\partial\Psi}{\partial I_6} + \frac{\partial\Psi}{\partial I_9} + \frac{3}{2}\frac{\partial\Psi}{\partial I_{10}} \right) \right. \right. \\ &\quad \left. \left. + 2\left(2\left(\frac{\partial\Psi}{\partial I_7} \right)^2 + \frac{\partial\Psi}{\partial I_6} \left(\frac{\partial\Psi}{\partial I_7} + \frac{\partial\Psi}{\partial I_8} \right) + 6\frac{\partial\Psi}{\partial I_7} \frac{\partial\Psi}{\partial I_8} + \frac{\partial\Psi}{\partial I_7} \frac{\partial\Psi}{\partial I_9} + 5\frac{\partial\Psi}{\partial I_8} \frac{\partial\Psi}{\partial I_8} + 2\frac{\partial\Psi}{\partial I_8} \frac{\partial\Psi}{\partial I_9} \right) \right] \right\}_{\gamma=0}. \end{aligned} \quad (32)$$

Notice that the above two equations are valid for arbitrary values of the field \mathbf{h} and hence of magnetostriction.

3.2.4. Energy density function for small magnetic fields

The energy density function describing the MRE response for small magnetic fields requires up to second-order terms of the magnetization field \mathbf{M} . Consequently, linear terms of the invariants from I_6 to I_{10} are adequate for our purpose. However, due to the strong influence of the prestress on the magnetostriction results observed experimentally, nonlinear terms of the invariants I_1 and I_4 will be required, leading to the following expression for the energy density:

$$\Psi = \frac{G}{2} \left\{ C_1 \sum_{k=1}^5 d_{1k}(I_1 - 3)^k + C_4 \sum_{k=2}^4 d_{4k}(I_4 - 1)^k + C_6 \frac{I_6}{M_s^2} + C_7 \frac{I_7}{M_s^2} + C_8 \frac{I_8}{M_s^2} + C_9 \frac{I_9}{M_s^2} + C_{10} \frac{I_{10}}{M_s^2} \right\}. \quad (33)$$

The evaluation of the coefficients in (33) is carried out with the following sequence:

- Using the $M-h$ initial slope in the experimental curve corresponding to the $\mathbf{h} \parallel \mathbf{N}$ tests for $\sigma/G = 0$ in Fig. 3a, we extract the coefficient C_9 .
- Using the $M-h$ initial slope in the experimental curve corresponding to the $\mathbf{h} \perp \mathbf{N}$ tests for $\sigma/G = -0.192$ in Fig. 3b, we extract the coefficient C_6 .
- Using the $\Delta\varepsilon-h$ initial curvature in the experimental curve corresponding to the $\mathbf{h} \parallel \mathbf{N}$ tests for $\sigma/G = 0$ and $\sigma/G = -0.192$ in Fig. 4a, we extract a coupled linear system for the coefficients C_7 and C_{10} .
- Using the $\Delta\varepsilon-h$ initial curvature in the experimental curve corresponding to the $\mathbf{h} \perp \mathbf{N}$ tests for $\sigma/G = -0.192$ in Fig. 4b, we extract the coefficient C_8 .
- Using the entire $\tau-\gamma$ curve in Fig. 7 for zero applied nondimensional magnetic field h/ρ_0M_s , we fit the constants, C_1 and d_{1k} (with $k=1,5$).
- Using the $\Delta\varepsilon-h$ initial curvature in the experimental curve corresponding to the $\mathbf{h} \parallel \mathbf{N}$ tests for $\sigma/G = 0.192$ in Fig. 4a, we extract the coefficient C_4 , whereas the constants d_{4k} ($k=2,4$) are obtained using the numerical results presented in Appendix.

The computed values for these coefficients are

$$C_1 = 1, \quad d_{11} = 1, \quad d_{12} = -7, \quad d_{13} = 120, \quad d_{14} = -700, \quad d_{15} = 3000,$$

$$C_4 = 0.103, \quad d_{42} = 1, \quad d_{43} = -21, \quad d_{44} = 90,$$

$$C_6 = 0.36, \quad C_7 = -0.32, \quad C_8 = 0.108, \quad C_9 = -0.12, \quad C_{10} = 0.075. \quad (34)$$

Notice in (34) that two of the coefficients, C_7 and C_9 are negative. Nevertheless, the overall energy density Ψ remains always positive, since $C_6 > C_9$ (with $I_9 = I_6$ for $\mathbf{h} \parallel \mathbf{N}$ and $I_9 = 0$ for $\mathbf{h} \perp \mathbf{N}$) and $C_6 + C_7\mathbf{C} + C_8\mathbf{C}^2 > 0$ for all \mathbf{C} . The constants C_4 ,

C_9 and C_{10} are non-zero due to the presence of particle chains. Values of these constants depend strongly on details of the particle chain geometry, which is obtained by varying the curing magnetic fields (see Chen et al., 2007). On the other hand, when the particles are distributed isotropically in the MRE, all the terms that depend on the orientation vector \mathbf{N} should be set equal to zero, i.e., $C_4 = C_9 = C_{10} = 0$.

Theoretical predictions, based on the energy density of Eq. (33), evaluated for the coefficients in (34), are compared to experimental results in the case of small to moderate magnetic fields in Figs. 8–10. More specifically, Fig. 8 shows the comparison between experiments (discrete symbols, for three different prestresses σ/G) and theory (continuous straight lines, in view of the quadratic dependence of the energy density Ψ on magnetization \mathbf{M}) for the dimensionless magnetization M/M_s versus applied nondimensional magnetic field $h/\rho_0 M_s$. The model captures fairly accurately the different initial slopes of the magnetization versus magnetic field curves for the two different particle chain alignments ($\mathbf{h} \parallel \mathbf{N}$ and $\mathbf{h} \perp \mathbf{N}$) as well as the small influence of prestress on these slopes. It is also worth mentioning that for $\mathbf{h} \perp \mathbf{N}$, the $M-h$ response is linear for $h/\rho_0 M_s$ up to the value of 0.4, while for $\mathbf{h} \parallel \mathbf{N}$ deviations of the $M-h$ response from linearity occur for lower nondimensional magnetic fields $h/\rho_0 M_s$ for values of about 0.25.

In Fig. 9, we show the comparison between experiments (discrete symbols for different prestresses) and theory (continuous lines for the parabolic $\Delta\varepsilon-h$ curves in view of the quadratic dependence of the energy density Ψ on magnetization \mathbf{M}) for the magnetostrictive strain $\Delta\varepsilon$ as a function of the applied nondimensional magnetic field $h/\rho_0 M_s$. More specifically, the applied nondimensional magnetic field $h/\rho_0 M_s$ is parallel to the particle chain orientation in Fig. 9a and perpendicular in Fig. 9b. Once again the theoretical model, which is fitted using three experiments from the parallel case shown in Fig. 9a (i.e., $\sigma/G = 0, \pm 0.192$ for $\mathbf{h} \parallel \mathbf{N}$) and one experiment from the perpendicular case shown in Fig. 9b (i.e., $\sigma/G = -0.192$ for $\mathbf{h} \perp \mathbf{N}$), predicts the remaining experimental results.

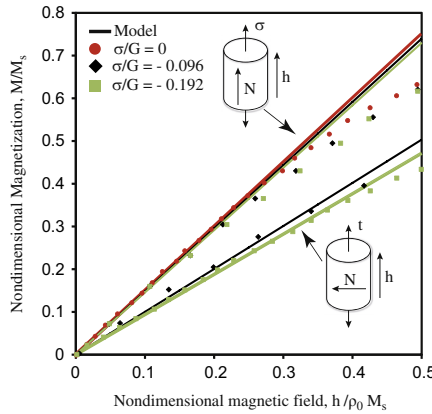


Fig. 8. Comparison for small magnetic fields between experimental (discrete symbols) and modeling (continuous lines) results for the nondimensional magnetization M/M_s versus the applied nondimensional magnetic field $h/\rho_0 M_s$ for various prestresses, σ/G , and orientations of the particle chains ($\mathbf{h} \parallel \mathbf{N}$ and $\mathbf{h} \perp \mathbf{N}$).

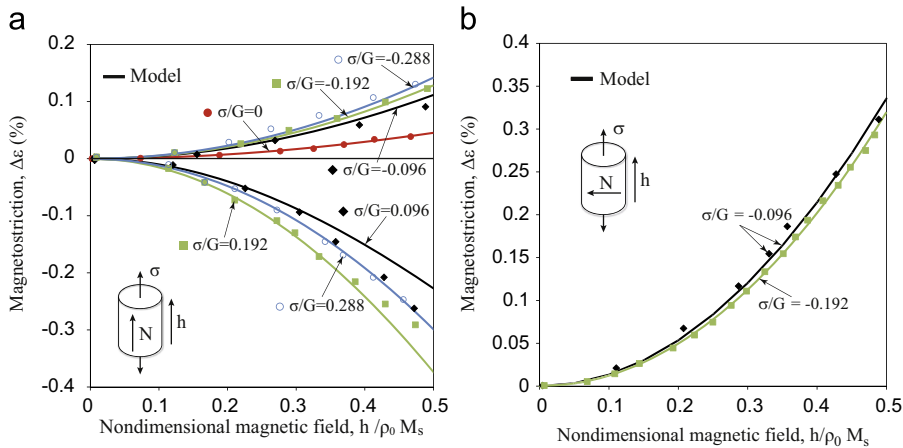


Fig. 9. Comparison for small magnetic fields between experimental (discrete symbols) and modeling (continuous lines) results for the magnetostriction $\Delta\varepsilon$ versus the applied nondimensional magnetic field $h/\rho_0 M_s$ for various prestresses, σ/G , aligned with the applied magnetic field. Part (a) and (b) correspond to the cases where the particle chains are parallel ($\mathbf{h} \parallel \mathbf{N}$) and perpendicular ($\mathbf{h} \perp \mathbf{N}$), respectively, to the applied magnetic field.

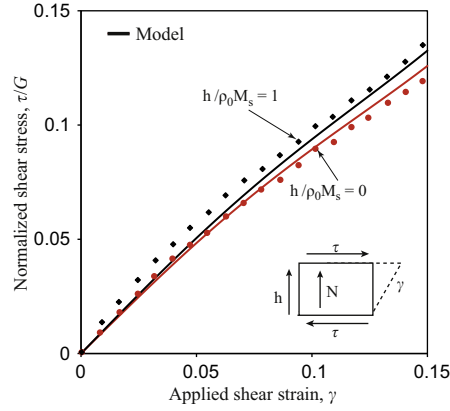


Fig. 10. Comparison between the experimental (discrete symbols) and modeling (continuous lines) stress versus strain results for simple shear in the absence or in the presence of a nondimensional magnetic field $h/\rho_0 M_s$. The particle chains are initially aligned to the applied magnetic field ($\mathbf{h} \parallel \mathbf{N}$ initially).

In Fig. 10, we observe that the model is able to reproduce adequately the entire τ – γ response in both cases of zero and non-zero applied magnetic field, even though the initial slope for $h/\rho_0 M_s = 1$ is not very well captured in this case. It should be mentioned here that in the shear experiment the resulting magnetizations have a moderate magnitude, i.e., $M_1/M_s \approx 0.6$ and $M_2/M_s \approx 0.03$ and hence the energy density without saturation, defined in (33), is sufficient for the description of this case.

3.3. Constitutive response for large magnetic fields

In order to account for magnetic saturation, i.e., for the nonlinear part of the M – h curves of the MRE response in Fig. 3 and the non-quadratic part of the $\Delta\varepsilon$ – h curves in Fig. 4, the energy density function (33) needs to be modified. To this end, in order to better approximate the experimental results at nondimensional magnetic fields $h/\rho_0 M_s > 0.5$, the energy function Ψ , defined in (33), is augmented by the following term:

$$\Psi_{sat} = \Psi + \frac{G}{2} \left\{ \left[-0.1216 \left(\frac{I_6}{I_7} - \frac{I_9}{I_7} \right) + 0.167 \left(\frac{I_6}{I_8} - \frac{I_9}{I_8} \right) \right] \left(\frac{I_6}{M_s^2} \right)^{1.5} + 0.083 \left(\frac{I_9}{I_7} \right)^{5.3} \left(\frac{I_6}{M_s^2} \right)^{2.8} \right\} \\ \times \left\{ \frac{1}{2} \ln \left[1 - \left(\frac{I_6}{M_s^2} \right)^2 \right] + \frac{I_6}{M_s^2} \tanh^{-1} \left(\frac{I_6}{M_s^2} \right) \right\}. \quad (35)$$

The motivation for the last term in bracket is that, in the absence of mechanical interactions, the predicted M – h response behaves as M – $\tanh(M)$, thus giving good fit with experimental observations near magnetic saturation. The additional non-quadratic I_6 and I_9 terms in (35) are added to improve the non-quadratic magnetostriction response at larger magnetic fields ($h/\rho_0 M_s > 0.5$). In view of this, the function (35) is found to give sufficiently good predictions for the M – h and $\Delta\varepsilon$ – h experiments up to $h/\rho_0 M_s = 1$, as shown in Figs. 11 and 12, respectively.

In particular, Fig. 11 compares M – h experimental and modeling curves that include magnetization saturation for several prestresses $\sigma/G \leq 0$. Part (a) corresponds to particle chains oriented along the applied magnetic field ($\mathbf{h} \parallel \mathbf{N}$), while part (b) compares results from part (a) with results obtained for the case where the particle chains are perpendicular to the applied magnetic field ($\mathbf{h} \perp \mathbf{N}$) with prestresses $\sigma/G < 0$. The agreement of the model is adequate for the entire range of the magnetic fields applied, while the saturation part is well described by the functional proposed in (35).

Fig. 12 compares $\Delta\varepsilon$ – h experimental and modeling curves that include magnetization saturation for several prestresses σ/G . Part (a) corresponds to particle chains oriented along the applied magnetic field ($\mathbf{h} \parallel \mathbf{N}$), while part (b) compares results from part (a) with results obtained for the case where the particle chains are perpendicular to the applied magnetic field ($\mathbf{h} \perp \mathbf{N}$) with prestresses $\sigma/G < 0$. The model predicts qualitatively the $\Delta\varepsilon$ – h curves in both parts although quantitatively is less accurate.

3.4. Quasiconvexity of the free energy function

Like in the case of finite elasticity, it is important to investigate the possibility of locally discontinuous solutions appearing in this coupled problem at adequately large magnetic and mechanical loads. The absence of such discontinuous solutions is ensured when the solid's potential energy is “quasiconvex”. This property requires that any arbitrary subregion $D \subset V$ of the solid with homogeneous (i.e., position independent) properties and under constant strain and

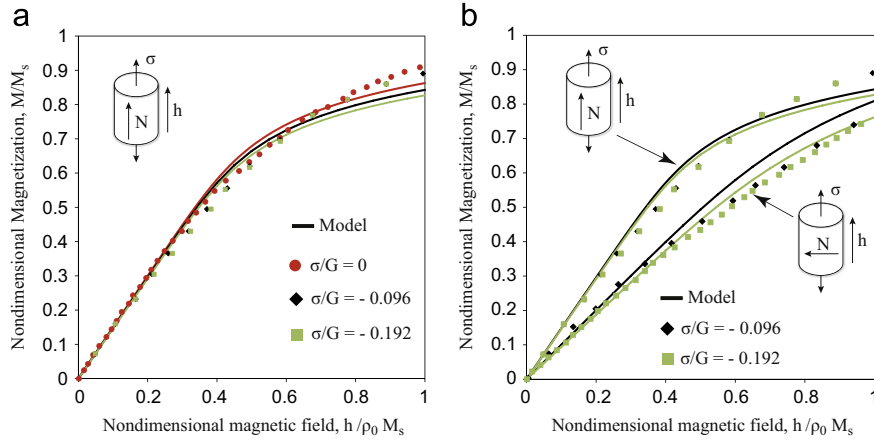


Fig. 11. Comparison for large magnetic fields between experiments (discrete symbols) and modeling that includes magnetization saturation effects (continuous lines) for the nondimensional magnetization M/M_s versus the applied nondimensional magnetic field $h/\rho_0 M_s$ for various prestresses σ/G . Part (a) corresponds to particle chains parallel to the applied magnetic field ($\mathbf{h} \parallel \mathbf{N}$) and part (b) shows the effect of particle chain orientation relative to the applied magnetic field ($\mathbf{h} \parallel \mathbf{N}$ and $\mathbf{h} \perp \mathbf{N}$).

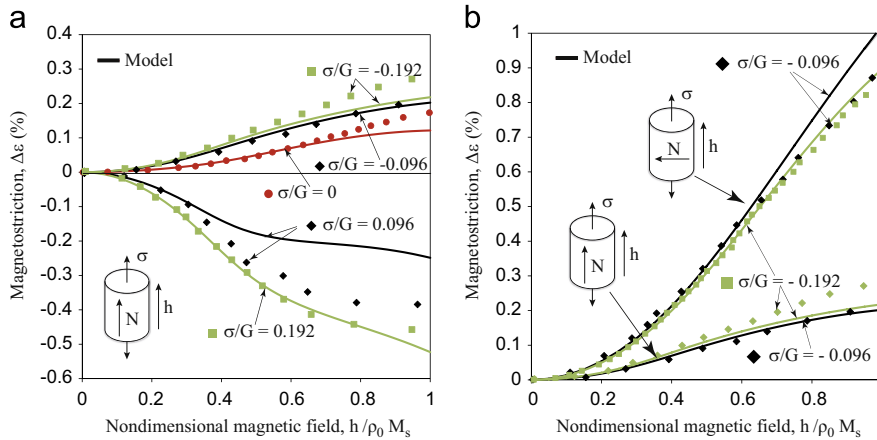


Fig. 12. Comparison for large magnetic fields between experiments (discrete symbols) and modeling that includes magnetization saturation effects (continuous lines) for the magnetostriction $\Delta \epsilon$ versus the applied nondimensional magnetic field $h/\rho_0 M_s$ for various prestresses, σ/G , aligned with the applied magnetic field. Part (a) corresponds to particle chains parallel to the applied magnetic field ($\mathbf{h} \parallel \mathbf{N}$) and part (b) shows the effect of the orientation of the particle chains relative to the applied magnetic field ($\mathbf{h} \parallel \mathbf{N}$ and $\mathbf{h} \perp \mathbf{N}$).

constant magnetization, has the lowest potential energy compared to all other states with admissible fields that satisfy Dirichlet conditions at the boundary ∂D .

Necessary pointwise conditions for the quasiconvexity of the energy function Ψ are derived by Kankanala and Triantafyllidis (2004) and require that the two following independent inequalities are satisfied:

$$(\mathbf{ab}) \bullet \bullet \left\{ \frac{\partial^2 \Psi}{\partial \mathbf{F} \partial \mathbf{F}} - \frac{\partial^2 \Psi}{\partial \mathbf{F} \partial \mathbf{M}} \bullet \left(\frac{\partial^2 \Psi}{\partial \mathbf{M} \partial \mathbf{M}} \right)^{-1} \bullet \frac{\partial^2 \Psi}{\partial \mathbf{M} \partial \mathbf{F}} \right\} \bullet \bullet (\mathbf{ab}) \geq 0, \quad \mathbf{a} \bullet \frac{\partial^2 \Psi}{\partial \mathbf{M} \partial \mathbf{M}} \bullet \mathbf{a} \geq 0, \quad (36)$$

where \mathbf{a} and \mathbf{b} are arbitrary real vectors. In the present study, due to the material incompressibility, the vectors \mathbf{a} and \mathbf{b} are not independent and they must satisfy the incremental incompressibility constraint:

$$\mathbf{a} \bullet \mathbf{F}^{-1} \bullet \mathbf{b} = 0. \quad (37)$$

Given the fact that the MRE under investigation is anisotropic, we expect that it will lose its rank one convexity when subjected to adequately large compressive stresses even in the absence of magnetization (see Agoras et al., 2009; Lopez-Pamies et al., 2010). Investigating the entire strain and magnetization space to find when the MRE at hand violates (36) is a daunting, if not a superfluous task. For the present work, it suffices to find the limits of quasiconvexity for the case of a uniaxial loading in the direction of the particle chain orientation under a field \mathbf{h} parallel to the particle chain. More specifically, we will establish the lowest stretch ratio λ_{cr} and corresponding stress σ_{cr}/G for which (36)₁ (note: (36)₂ always satisfied) fails along a loading path given in (10) for different applied fields \mathbf{h} .

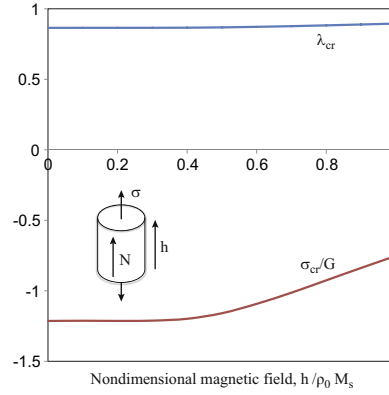


Fig. 13. Critical values for stretch λ_{cr} and related axial stress σ_{cr}/G corresponding to the loss of quasiconvexity in a uniaxial loading experiment with $\mathbf{h} \parallel \mathbf{N}$ as a function of the applied magnetic field.

In general, any unit vector can be written as a function of two (not uniquely defined) Euler angles, i.e.,

$$\mathbf{a} = \sin \phi_1 \cos \phi_2 \mathbf{e}_1 + \sin \phi_1 \sin \phi_2 \mathbf{e}_2 + \cos \phi_1 \mathbf{e}_3, \tag{38}$$

with $\phi_1 \in [0, \pi)$ and $\phi_2 \in [0, 2\pi)$. The second vector \mathbf{b} must satisfy the incompressibility constraint (37), hence only one additional Euler angle is needed for its definition. Consequently, for convenience, for convenience, we define a new vector $\tilde{\mathbf{b}}$, which is perpendicular to \mathbf{a} , i.e., $\mathbf{a} \cdot \tilde{\mathbf{b}} = 0$, by

$$\tilde{\mathbf{b}} = (\cos \phi_1 \cos \phi_2 \cos \phi_3 - \sin \phi_2 \sin \phi_3) \mathbf{e}_1 + (\cos \phi_1 \sin \phi_2 \cos \phi_3 + \cos \phi_2 \sin \phi_3) \mathbf{e}_2 - \sin \phi_1 \cos \phi_3 \mathbf{e}_3, \tag{39}$$

with $\phi_3 \in [0, 2\pi)$. It should be noted that the previous definition for $\tilde{\mathbf{b}}$ is not unique since any vector lying on the plane defined by the normal \mathbf{a} (given in (38)) would be appropriate. Subsequently, by setting $\mathbf{b} = \mathbf{F} \cdot \tilde{\mathbf{b}}$, one readily satisfies the constraint (37). It should be noted that in the last definition \mathbf{b} does not have a unit magnitude, however this does not affect our calculations since the sign of (36)₁ depends only upon the orientation of the vectors \mathbf{a} and \mathbf{b} . Then a complete scan is carried out for $0 \leq \phi_1, \phi_3 < 2\pi$ and $0 \leq \phi_2 < \pi$ using an increment of $\Delta\phi_1 = \Delta\phi_2 = \Delta\phi_3 = \pi/180$.

The results in Fig. 13 show that although the MRE model used in (35) is not quasiconvex, its quasiconvexity is lost for rather large values of the compressive stress, which are considerably higher than the maximum ones used experimentally ($|\sigma/G| \leq 0.288$). It is also worth mentioning that the compressive stresses required for loss of quasiconvexity diminish with increasing h , while no loss of quasiconvexity occurs for tensile stresses.

In contrast, the function Ψ given by (35) remains quasiconvex for the entire range of applied deformations (tensile and compressive) and magnetic fields in the cases of uniaxial stretching where the particle chains are perpendicular to the applied magnetic field and the applied traction direction, and in the simple shear loading where the particle chains are initially parallel to the applied magnetic field and perpendicular to the shearing direction.

4. Conclusions

In this work, we present a combined experimental and theoretical study of the macroscopic response of a particular MRE consisting of a rubber matrix phase with spherical carbonyl iron particles. The MRE specimens used in this study are cured in the presence of strong magnetic fields leading to the formation of particle chain structures and thus to an overall transversely isotropic response of the composite. The MRE samples are tested experimentally under uniaxial stresses as well as under simple shear in the absence or in the presence of magnetic fields and for different initial orientations of their particle chains with respect to the mechanical and magnetic loading direction.

Our experiments show that the initial orientation of the particle chains has a significant effect on both the magnetization and the magnetostriction responses of the MRE. Moreover, we observe a strong dependence of the magnetostriction on the applied prestress, while no effect of prestress is detected on the magnetization response. More specifically, for zero or compressive prestresses the experimentally measured magnetostriction leads to an overall elongation of the MRE. In contrast, by switching the sign of the prestress to a sufficiently large tensile value, we observe a change in the sign of the magnetostriction leading to an overall contraction of the MRE along the applied magnetic field direction.

These counterintuitive effects are attributed to two important mechanisms. The MRE elongation at zero or negative prestress along the applied magnetic field direction is explained by the presence of the restoring force between a pair of particles that are non-aligned with the applied magnetic field, a mechanism originally suggested by Klingenberg and Zukoski (1990) in the context of electrorheological suspensions and later by Lemaire and Bossis (1991) and Bossis and Lemaire (1991) in the context of magnetic suspensions. The nonlinear dependence of the magnetostriction on the applied prestress is attributed to the strong tension–compression asymmetry of the purely mechanical constitutive response of the MRE even at relatively small macroscopic strains (in the order of 2–5%) which is a direct consequence of the particle chain microstructure.

Using the theoretical framework introduced by Kankanala and Triantafyllidis (2004) for finitely strained MRE's, we model the experimentally measured initial magnetization slopes and initial magnetostriction curvatures with the help of a transversely isotropic energy function which depends on seven invariants (out of the maximum ten that are theoretically available), two purely mechanical and five magnetomechanical ones, in an additive manner. In order to capture the inherent nonlinear tension–compression asymmetry of the MRE present even at relatively small macroscopic strains, a nonlinear dependence of the energy function on the two mechanical invariants is adopted. The remaining terms of the energy density, which have a quadratic dependence on the magnetization, are calculated from a subset of the magnetization and magnetostriction experimental data. The constructed energy density is found to accurately predict the remaining experimental initial magnetization slopes and initial magnetostriction curvatures. The same experimentally obtained energy density is able to model the simple shear response in the absence or in the presence of a magnetic field.

The above-mentioned additive energy function is then augmented with a non-quadratic term on the magnetization in order to model the magnetization saturation response of the MRE. The corresponding energy density function is found to be adequate when compared with the existing experimental results at large magnetic fields. The quasiconvexity of the proposed energy function is also checked along the loading paths considered in the experiments. It is found that only in the case where the particle chains are aligned with the magnetic field and the specimen is subject to compression along the same direction, the material violates the quasiconvexity conditions and the MRE sample is prone to localization of deformation. However, the computed critical loads for the violation of quasiconvexity are considerably larger than the experimentally applied ones, which is in accord with the experimental observations that show no evidence of localized deformations.

The present experimental/theoretical investigation for MREs subjected to coupled mechanical and magnetic loading gives an excellent agreement with experiments up to relatively moderate magnetic fields and is satisfactorily extended to include magnetic fields near saturation. The work shows the adequacy of the anisotropic, finite strain continuum formulation for the description of these materials. The study also demonstrates the importance of microgeometry in the macroscopic magnetoelastic coupling response of the composite. Given the need in applications to produce MREs with strong magnetoelastic coupling, it is desirable to build (a) microscopic models to study these coupling mechanisms in detail and (b) mean-field (i.e., homogenization) models to investigate more efficiently the influence of matrix properties, particle distribution and shape on the macroscopic magnetomechanical response of these composites. On the practical side, mean field theories are a valuable tool to optimize coupling properties (e.g., Kuo et al., 2010; Corcolle et al., 2009) in these materials. Studies in these directions are currently under way by the authors.

Acknowledgements

K.D. acknowledges the support of the Solid Mechanics Laboratory of the Ecole Polytechnique and the Centre National de la Recherche Scientifique (C.N.R.S.). S.K. would like to thank Dr. John Ginder of Ford Motor Company for his guidance and help with the experimental part of the work. S. K. would also like to acknowledge Dr. Mark Nichols of Ford Motor Company for providing the needed samples for the experiments. N.T. gratefully acknowledges partial support from the National Science Foundation, grant DMI 0400143 and the support of the Foundation of the Ecole Polytechnique.

Appendix A. Mechanical response for particle chain reinforced elastomers

In order to assess the effect of the particle chain microgeometry on the macroscopic mechanical constitutive response of the MRE, we carry out the following numerical (FEM) calculations. A cylindrical unit-cell is introduced as an approximation to a hexagonal-cross-section unit-cell of a periodic neo-Hookean elastomer where the rigid spherical inclusions are aligned in parallel chains, as shown schematically in Fig. 14. This allows the reduction of a three-dimensional geometry to an axisymmetric one, provided that the loads applied preserve the axisymmetric character of the problem (see Găărăjeu et al., 2000).

In the FEM simulations a single spherical particle is placed at the center of the unit cell, as shown in Fig. 14. By adjusting the magnitude of H_c for a given cell ratio H_c/R_c and particle radius R_i , we obtain the experimentally relevant particle volume fraction of $f = 25\%$.

Next, we consider a nearly incompressible neo-Hookean matrix phase (shear modulus G and bulk modulus $\kappa = 10^5 G$), while the particle is modeled as rigid by imposing zero displacement conditions at the interface between the particle and the matrix phase. The unit cell is subjected to uniaxial stretching with stretch ratio λ along the symmetry axis- Z , such that the displacement field \mathbf{u} can be split into a homogeneous part and a correction \mathbf{u}^* , i.e.,

$$u_R = (\lambda^{-1/2} - 1)R + u_R^*(R, Z), \quad u_Z = (\lambda - 1)Z + u_Z^*(R, Z), \quad (\text{A.1})$$

where R, Z denote the reference cylindrical coordinates in an attempt to model as closely as possible the overall incompressibility of the composite material. In order to approximate as closely as possible the periodicity met in a cylinder with hexagonal cross-section, we impose the following boundary condition on the outer boundaries of the unit cell (Găărăjeu et al., 2000):

$$u_R^*(R = R_c, Z) = u_Z^*(R, Z = H_c) = 0. \quad (\text{A.2})$$

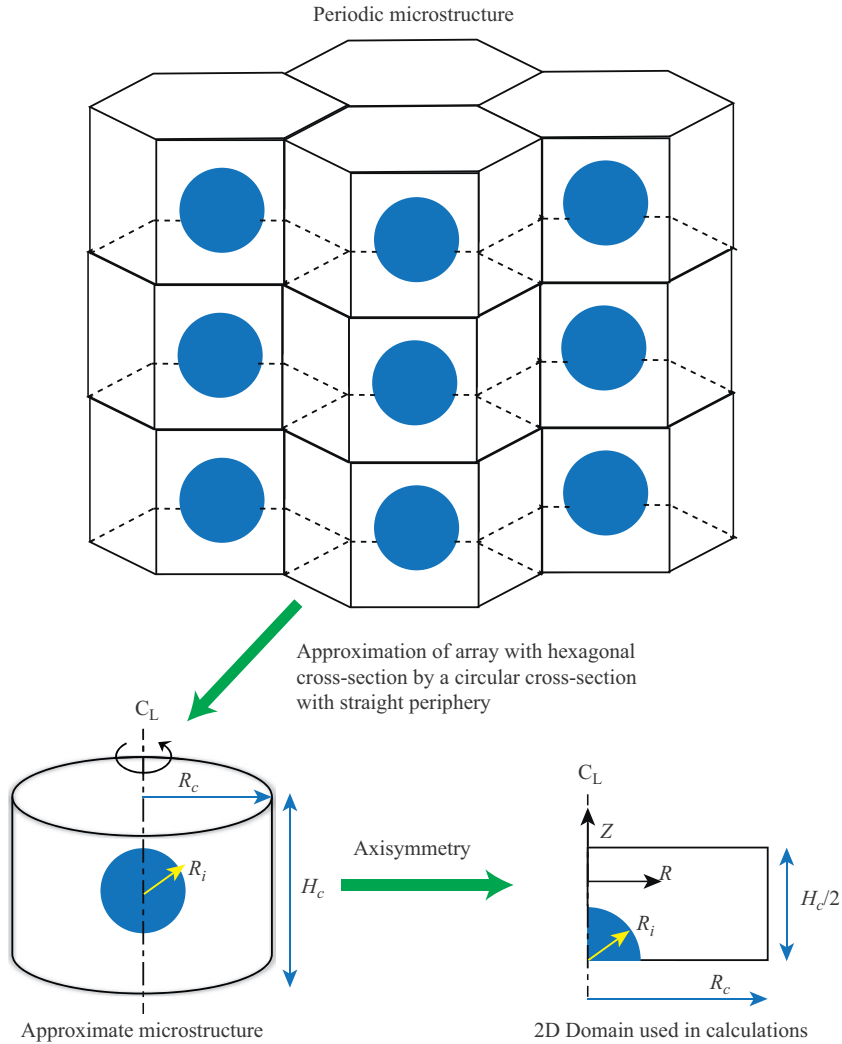


Fig. 14. Approximation of a three-dimensional periodic neo-Hookean elastomer reinforced by spherical particles aligned in parallel chains. The hexagonal-cross-section unit cell is approximated by a cylindrical one with circular cross-section. This procedure is valid only for axisymmetric loading conditions with respect to the particle chain orientation.

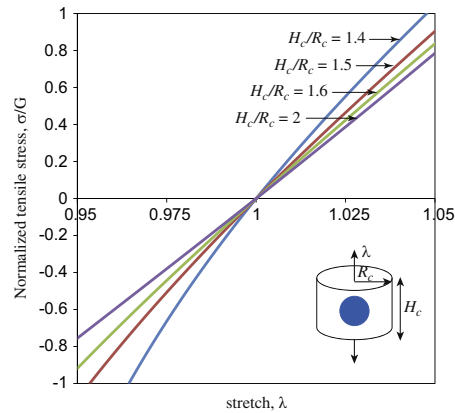


Fig. 15. Normalized tensile stress σ/G versus stretch ratio λ for various values of the unit cell aspect ratio H_c/R_c . The cylindrical unit cell is subjected to isochoric stretching along the symmetry axis, while its external surface $R = R_c$ remains straight. The radius of the rigid particle R_i is computed such that the volume fraction in the host elastomer (neo-Hookean with shear modulus G) is equal to 25% for any given ratio H_c/R_c .

The geometrical interpretation of this boundary condition is that the unit cell remains a cylinder with a circular cross-section and an average strain given by (10)₁, as described in Section 3.2.1.

Fig. 15 shows normalized tensile stress σ/G as a function of the applied stretch ratio λ for several cell aspect ratios $H_c/R_c = 1.4, 1.5, 1.6, 2$. It is clear from this figure that as H_c/R_c decreases, the particles become more aligned yielding a transversely isotropic overall response along the Z-direction. More interestingly, as we decrease the interparticle distance in the chain (by reducing H_c/R_c), the response of the material becomes very nonlinear even at small stretch ratios $\lambda = 1.02–1.05$ (i.e., strains 2–5%) exhibiting a strong tension–compression asymmetry. This tension–compression asymmetry has been shown to be crucial in capturing the nonlinear effect of the prestress on the magnetostriction response of the MRE, as described in the main text (see Figs. 4 and 9 and relevant discussion). In addition, the $H_c/R_c = 1.4$ curve in Fig. 15 has been used to extract the d_{4k} (with $k=2,4$) constants used in the definition of the free energy function (33).

References

- Adkins, J., 1959. Symmetry relations for orthotropic and transversely isotropic materials. *Arch. Ration. Mech. Anal.* 4, 193–213.
- Adkins, J., 1960. Further symmetry relations for transversely isotropic materials. *Arch. Ration. Mech. Anal.* 5, 263–274.
- Agoras, M., Lopez-Pamies, O., Ponte Castañeda, P., 2009. Onset of macroscopic instabilities in fiber-reinforced elastomers at finite strain. *J. Mech. Phys. Solids* 57, 1828–1850.
- Bellan, C., Bossis, G., 2002. Field dependence of viscoelastic properties of mr elastomers. *Int. J. Mod. Phys. B* 16, 2447–2453.
- Borcea, L., Bruno, O., 2001. On the magneto-elastic properties of elastomer-ferromagnet composites. *J. Mech. Phys. Solids* 49, 2877–2919.
- Bossis, G., Lemaire, E., 1991. Yield stresses in magnetic suspensions. *J. Rheol.* 35, 1345–1354.
- Brigadnov, I.A., Dorfmann, A., 2003. Mathematical modeling of magneto-sensitive elastomers. *Int. J. Solids Struct.* 40, 4659–4674.
- Brown, W.F., 1966. *Magnetoelastic Interactions*. Springer-Verlag, New York.
- Chen, L., Gong, X.L., Li, W.H., 2007. Microstructures and viscoelastic properties of anisotropic magnetorheological elastomers. *Smart Mater. Struct.* 16, 2645–2650.
- Coquelle, E., Bossis, G., Szabo, D., Giulieri, F., 2006. Micromechanical analysis of an elastomer filled with particles organized in chain-like structure. *J. Mater. Sci.* 41, 5941–5953. [10.1007/s10853-006-0329-8](https://doi.org/10.1007/s10853-006-0329-8).
- Corcolle, R., Daniel, L., Bouillault, F., 2008. Optimal design of magnetostrictive composites: an analytical approach. *IEEE Trans. Magn.* 44, 17–23.
- Corcolle, R., Daniel, L., Bouillault, F., 2009. Intraphase fluctuations in heterogeneous magnetic materials. *J. Appl. Phys.* 105, 123913.
- deBotton, G., Hariton, I., Socolsky, E., 2006. Neo-Hookean fiber-reinforced composites in finite elasticity. *J. Mech. Phys. Solids* 54, 533–559.
- Diguet, G., Beaunon, E., Cavaillé, J., 2010. Shape effect in the magnetostriction of ferromagnetic composite. *J. Magn. Magn. Mater.* 322, 3337–3341.
- Dorfmann, A., Ogden, R.W., 2003. Magnetoelastic modelling of elastomers. *Eur. J. Mech. A/Solids* 22, 497–507.
- Gărăjeu, M., Michel, J.C., Suquet, P., 2000. A micromechanical approach of damage in viscoplastic materials by evolution in size, shape and distribution of voids. *Comput. Methods Appl. Mech. Eng.* 183, 223–246.
- Ginder, J., Clark, S., Schlotter, W., Nichols, M., 2002. Magnetostrictive phenomena in magnetorheological elastomers. *Int. J. Mod. Phys. B* 16, 2412–2418 (Eighth International Conference on Electro-Rheological Fluids and Magneto-Rheological Suspensions, Nice, France, July 09–13, 2001).
- Ginder, J., Nichols, M., Elie, L., Tardiff, J., 1999. Magnetorheological elastomers: properties and applications. In: M. Wuttig (Ed.), *Smart Structures and Materials 1999*, Proceedings of the SPIE, vol. 3675. Smart Materials Technologies, pp. 131–138.
- Gong, X.L., Zhang, X.Z., Zhang, P.Q., 2005. Fabrication and characterization of isotropic magnetorheological elastomers. *Polymer Testing* 24, 669–676.
- Jolly, M.R., Carlson, J.D., Muñoz, B.C., 1996. A model of the behaviour of magnetorheological materials. *Smart Mat. Struct.* 5, 607.
- Kankanala, S.V., 2007. On Finitely Strained Magnetoelastic Solids. Doctoral Dissertation, The University of Michigan, Ann Arbor.
- Kankanala, S.V., Triantafyllidis, N., 2004. On finitely strained magnetorheological elastomers. *J. Mech. Phys. Solids* 52, 2869–2908.
- Klingenberg, D.J., Zukoski, C.F., 1990. Studies on the steady-shear behavior of electrorheological suspensions. *Langmuir* 6, 15–24.
- Kovetz, A., 2000. *Electromagnetic Theory*. Oxford, New York.
- Kuo, H.Y., Slinger, A., Bhattacharya, K., 2010. Optimization of magnetoelectricity in piezoelectric–magnetostrictive bilayers. *Smart Materials and Structures* 19, 125010.
- Lemaire, E., Bossis, G., 1991. Yield stress and wall effects in magnetic colloidal suspensions. *J. Phys. D: Appl. Phys.* 24, 1473.
- Liu, L., James, R., Leo, P., 2006. Magnetostrictive composites in the dilute limit. *J. Mech. Phys. Solids* 54, 951–974.
- Lopez-Pamies, O., Idiart, M., Li, Z., 2010. On microstructure evolution in fiber-reinforced elastomers and implications for their mechanical response and stability. *J. Eng. Math.* 68, 57–83.
- Maugin, G.A., Eringen, A.C., 1972a. Deformable magnetically saturated media. i. Field equations. *J. Math. Phys.* 13, 143–155.
- Maugin, G.A., Eringen, A.C., 1972b. Deformable magnetically saturated media. ii. Constitutive theory. *J. Math. Phys.* 13, 1334–1347.
- Moffett, M.B., Clark, A.E., Wun-Fogle, M., Linberg, J., Teter, J.P., McLaughlin, E.A., 1991. Characterization of Terfenol-D for magnetostrictive transducers. *J. Acoust. Soc. Am.* 89, 1448–1455.
- Pao, Y.H., 1978. Electromagnetic forces in deformable continua. In: Nemat-Nasser, S. (Ed.), *Mechanics Today*, Pergamon Press, Inc, New York, pp. 209–305.
- Pao, Y.H., Yeh, C.S., 1973. A linear theory for soft ferromagnetic elastic solids. *Int. J. Eng. Sci.* 11, 415–436.
- Pipkin, A., Rivlin, R., 1959. The formulation of constitutive equations in continuum physics. i. *Arch. Ration. Mech. Anal.* 4, 129–144.
- Ponte Castañeda, P., Galipeau, E., 2011. Homogenization-based constitutive models for magnetorheological elastomers at finite strain. *J. Mech. Phys. Solids* 59, 194–215.
- Rigbi, Z., Jilkén, L., 1983. The response of an elastomer filled with soft ferrite to mechanical and magnetic influences. *J. Magn. Magn. Mater.* 37, 267–276.
- Tiersten, H.F., 1964. Coupled magnetomechanical equations for magnetically saturated insulators. *J. Math. Phys.* 5, 1298–1318.
- Tiersten, H.F., 1965. Variational principle for saturated magnetoelastic insulators. *J. Math. Phys.* 6, 779–787.
- Truesdell, C., Toupin, R., 1960. The classical field theories. In: Flügge, S. (Ed.), *Handbuch der Physik*, Springer-Verlag, Berlin.
- Yin, H., Sun, L., Chen, J., 2006. Magneto-elastic modeling of composites containing chain-structured magnetostrictive particles. *J. Mech. Phys. Solids* 54, 975–1003.